



**HAL**  
open science

## Estimating channel parameters and discharge at river network scale using hydrological-hydraulic models, SWOT and multi-satellite data

Kévin Larnier, Pierre-André Garambois, Charlotte Emery, Léo Pujol, Jérôme Monnier, Laetitia Gal, Adrien Paris, Hervé Yesou, Thomas Ledauphin, Stéphane Calmant

### ► To cite this version:

Kévin Larnier, Pierre-André Garambois, Charlotte Emery, Léo Pujol, Jérôme Monnier, et al.. Estimating channel parameters and discharge at river network scale using hydrological-hydraulic models, SWOT and multi-satellite data. 2025. hal-04681079v2

**HAL Id: hal-04681079**

**<https://hal.inrae.fr/hal-04681079v2>**

Preprint submitted on 23 Jan 2025

**HAL** is a multi-disciplinary open access archive for the deposit and dissemination of scientific research documents, whether they are published or not. The documents may come from teaching and research institutions in France or abroad, or from public or private research centers.

L'archive ouverte pluridisciplinaire **HAL**, est destinée au dépôt et à la diffusion de documents scientifiques de niveau recherche, publiés ou non, émanant des établissements d'enseignement et de recherche français ou étrangers, des laboratoires publics ou privés.

# Estimating channel parameters and discharge at river network scale using hydrological-hydraulic models, SWOT and multi-satellite data

Kévin Larnier<sup>1</sup>, Pierre-André Garambois<sup>2</sup>, Charlotte Emery<sup>3</sup>, Léo Pujol<sup>2</sup>, Jérôme Monnier<sup>4</sup>,  
Laetitia Gal<sup>1</sup>, Adrien Paris<sup>1</sup>, Hervé Yesou<sup>6</sup>, Thomas Ledauphin<sup>6</sup>, Stéphane Calmant<sup>1</sup>

<sup>1</sup>Hydro Matters, Toulouse, France

<sup>2</sup>INRAE, Aix-Marseille Université, RECOVER, Aix-en-Provence, France

<sup>3</sup>CS Group, Toulouse, France

<sup>4</sup>INSA, IMT, Toulouse, France

<sup>5</sup>CPRM, Brazil

<sup>6</sup>SERTIT, ICube, Strasbourg University, France

## Key Points:

- Calibration of Saint-Venant river network model using hydrological inputs and variational data assimilation of SWOT data at basin scale.
- Estimation of spatially-distributed inflow hydrographs, bathymetry, and friction across the river network.
- Automatic pre-processing of multi-satellite altimetry and images for basin scale model setup and wavelet-based filtering of SWOT L2 RiverSP data at node scale.

## Abstract

The unprecedented hydraulic visibility of rivers surfaces deformation with SWOT satellite offers tremendous information for improving hydrological-hydraulic (H&H) models and discharge estimations for rivers worldwide. However, estimating the uncertain or unknown parameters of hydraulic models, such as inflow discharges, bathymetry, and friction parameters, poses a high-dimensional inverse problem, which is ill-posed if based solely on altimetry observations. To address this, we couple the hydraulic model with a semi-distributed hydrological model, to constrain the ill-posed inverse problem with sufficiently accurate initial estimates of inflows at the network upstreams. A robust variational data assimilation (VDA) of water surface elevation (WSE) data into a 1D Saint-Venant river network model, enables the inference of inflow hydrographs, effective bathymetry, and spatially distributed friction at network scale. The method is demonstrated on the large, complex, and poorly gauged Maroni basin in French Guiana. The pre-processing chain enables (i) building an effective hydraulic model geometry from drifting ICESat-2 WSE altimetry and Sentinel-1 width; (ii) filtering noisy SWOT Level 2 WSE data before assimilation. A systematic improvement is achieved in fitting the assimilated WSE (85% cost improvement), and in validating discharge at 5 gauges within the network. For assimilation of SWOT data alone, 70% of data-model fit is in  $[-0.25 ; 0.25m]$

---

Corresponding author: Pierre-André Garambois, [pierre-andre.garambois@inrae.fr](mailto:pierre-andre.garambois@inrae.fr)

31 and the discharge NRMSE ranges between 0.05 and 0.18 (18% to 71% improvement from prior). The high density  
32 of SWOT WSE enables the inference of detailed spatial variability in channel bottom elevation and friction, and  
33 inflows timeseries. The approach is transferable to other rivers networks worldwide.

34 **Keywords:** Satellite data of SWOT, ICESat2 and Sentinel 3 altimetry, Sentinel 1 images; Saint-Venant River  
35 Network Model; Adjoint Model; Variational Data Assimilation; Discharge; Bathymetry; Friction; Spatio-temporal  
36 parameters; Inference; Estimation; Calibration; Hydrological-Hydraulic model; Sequential Coupling; Basin; Poorly  
37 gauged.

## 38 1 Introduction

39 Improving the estimation of freshwater stocks and fluxes in surface hydrology is crucial for advancing scientific  
40 knowledge of the earth system and addressing major socio-economic issues such as water resource management  
41 and forecasting extremes (floods and droughts), especially in the context of climate change and potential intensifi-  
42 cation of the water cycle (Masson-Delmotte et al., 2022). Developing detailed and reliable hydrological-hydraulic  
43 (H&H) models that can translate atmospheric signals into river flows, inundations depths, velocities, extents, while  
44 integrating available observations, is essential for scientific research and decision support. However, more complex  
45 modeling requires more information to constrain it effectively.

46  
47 Hydrological-hydraulic modeling typically requires data to describe (1) atmospheric forcings, (2) physical prop-  
48 erties of the catchment (drainage, topography, land use, soil and bedrock composition , etc) and the hydrographic  
49 network (bathymetry, hydraulic friction, structures), as well as flow observations (discharge and water depth at  
50 the very least, flow velocities, slopes, soil moisture, etc) to estimate the model parameters. Discharge data, which  
51 are crucial to calibrate a stage-discharge law or rainfall-runoff hydrological models, vary in availability depending  
52 on the basins and the spatial density of their ground measurement networks. These data integrate the complex  
53 signature of combined physical processes occurring in the compartments of the upstream basin (rivers, lakes, bio-  
54 sphere, aquifers and unsaturated soils, cf. Milly (1994)) with significant spatio-temporal variabilities (e.g. Flipo  
55 et al. (2014); Schuite et al. (2019)), and contain uncertainty (e.g. Mansanarez et al. (2016); Horner et al. (2018);  
56 Eggleston et al. (2024)). Bathymetry and friction data are essential for constraining hydraulic modeling but are  
57 often unavailable and remain unmeasurable from space. Dry bathymetry can be accurately measured with airborne  
58 LiDAR while wet bathymetry below river surface requires in situ surveys or penetrating LiDAR in clear, shallow  
59 streams (cf. Lague & Feldmann (2020)). Hydraulic model friction can only be estimated indirectly from flow  
60 measurements.

61 Complementing in situ data, new generations of Earth Observation (EO) satellites and sensors provide increasingly  
62 accurate and spatially dense measurements of water surface variabilities in worldwide rivers, especially on remote  
63 and hard-to-measure areas, including water surface elevation  $Z$ , width  $W$  and slope  $S$ .

This hydraulic visibility provided by single or multi-satellite measurements - *the potential to depict a hydrological response and surface hydraulic variabilities within a river section or network via remote sensing* (Garambois et al. (2017), see also Rodríguez et al. (2020)) - can offer valuable information for estimating discharge with local laws or spatialized hydraulic models that both require calibration of their parameters. Local algebraic laws can be stage-discharge rating curves  $Q = f(Z)$  (Paris et al., 2016) or width-discharge  $Q = f(W)$  (Pavelsky, 2014) or  $Q = f(Z, S, W)$  stage-fall-discharge (Malou et al., 2021) or Low Froude Manning-Strickler (Garambois & Monnier, 2015; Larnier et al., 2020). Spatialized hydraulic models can vary in complexity and range from reach scale to network scale (e.g. Getirana (2010); Paiva et al. (2013); Garambois et al. (2017); Schneider et al. (2017); Coppo Frias et al. (2022)).

For instance, the MGB model (Modelo de Grandes Bacias, (Collischon et al., 2007; Pontes et al., 2017)), using simplified 1D hydraulics, has been calibrated with ENVISAT data (Getirana, 2010; Paiva et al., 2013) and multi-satellite data (Meyer Oliveira et al., 2021). Other models, such as a simplified 1D hydraulic model of an anastomosed reach (Garambois et al., 2017), a 1D dynamic wave model (Schneider et al., 2017), a low-parameterized steady hydraulic model (Coppo Frias et al., 2022), have been calibrated using various nadir altimetry data. These studies used simplified cross-section shapes and classical global search algorithms for low-dimensional calibration problems. However, more advanced algorithms are required to estimate high-dimensional, spatially distributed parameters of complete hydraulic models, to approximate flow observations accurately while reducing modeling errors.

Nevertheless, the estimation of hydraulic model parameters from water surface (WS) observables can result in more or less difficult and ill-posed inverse problems. This difficulty depends on the complexity of the physical system, on the informative content carried by observations, which is linked to their nature and spatio-temporal distribution, on the employed physical model's capability to reproduce partially observed signals from the physical system, and on the sought parameters.

Starting from local physical considerations, at a section or at river reach scale, discharge  $Q$  of gradually varied flows (cf. Chow (1959); S. Dingman (2009)) can be related to flow energy slope  $S_f$  such that:

$$Q = \kappa S_f^{1/2} = \prod_{i=1}^N p_i^{\alpha_i} \quad (1)$$

where  $\kappa$  is the conveyance (S. Dingman, 2009), inversely proportional to a friction parameter  $\rho$  such that  $p_1 = 1/\rho$  and proportional to the product of the flow parameters  $p_i$  raised to the corresponding exponent  $\alpha_i$  (cf. S. Dingman (2009); Rodríguez et al. (2020)). Common friction parametrizations include those of Chézy, Manning-Strickler or Darcy-Weisbach (cf. Chow (1959); S. Dingman (2009)). These power laws can be related to rivers hydraulic-geometry (Leopold & Maddock, 1953), see analysis in S. L. Dingman & Afshari (2018); Eggleston et al. (2024) and references therein. Given the relatively large scales of satellite measurements, observed flows can be considered stationary and mainly Low Froude ( $Fr \leq 0.3$ ), where the friction slope  $S_f$  equals the surface slope  $S = |\partial_x Z| > 0$ . The low Froude Manning-Strickler equation applied with slope  $S$ , in its simplest form, (Garambois & Monnier,

98 [2015; Durand et al., 2014](#)) is:

$$Q = KAR_h^{2/3} \sqrt{S} \quad (2)$$

99 Where  $K$  is the Strickler friction coefficient,  $A$  and  $R_h$  are respectively the wetted flow section and hydraulic radius  
100 depending on bathymetry  $b$  and cross-section (XS) geometrical shape. Estimating discharge from WS observations  
101 with unknown bathymetry  $b$  and friction  $K$  embedded in the low Froude Manning-Strickler model, is an ill-posed  
102 inverse problem ([Larnier et al., 2020](#); [Garambois & Monnier, 2015](#)).

103 When reliable discharge data, from ground-based measurements or calibrated river network models, are available  
104 for estimating flow laws parameters, accurate discharge estimates can be achieved. The accuracy of satellite-based  
105 discharge estimate depends on observation errors, flow law parameters error and structural model errors [Yoon et](#)  
106 [al. \(2016\)](#); [Larnier et al. \(2020\)](#); [Durand et al. \(2023\)](#). Site-specific geomorphic and hydraulic conditions affect  
107 both ground-based (e.g. [Le Coz et al. \(2014\)](#); [Mansanarez et al. \(2016\)](#)) and satellite-based river flow monitoring  
108 ([Frasson et al., 2021](#); [Eggleston et al., 2024](#)).

109 It has been shown that the discharge inverse problem, based on hydrodynamic models and water surface (WS)  
110 measurements without additional priors, is mathematically ill-posed ([Larnier et al., 2020](#)). This crucial remark ex-  
111 plains the bias observed when using current algorithms for single river portions (see [Frasson et al. \(2021\)](#); [Durand et](#)  
112 [al. \(2023\)](#) and references therein). The bias depends on the employed physical equations, initial values of iterative  
113 algorithms, methodology priors, and other factors ([Larnier & Monnier, 2023](#)). The algorithms aiming at calibrat-  
114 ing complete space-time dependent flow models (typically Saint-Venant equations based system) need to infer the  
115 inflow discharge, bathymetry and friction parameters. After calibration via data assimilation (e.g. assimilation of  
116 synthetic SWOT data using VDA ([Pujol et al., 2020](#)) or Kalman filter ([Wongchuig-Correa et al., 2020](#))), accurate  
117 space-time variations of the signal can be retrieved, albeit with bias. This bias can be removed if considering accu-  
118 rate mean value of discharge or even reference value of one of the two other parameters (bathymetry, friction) as  
119 shown in [Larnier et al. \(2020\)](#). Several studies, based on sophisticated variational data assimilation processes ([Asch](#)  
120 [et al., 2016](#); [Monnier, 2021](#)) have been developed, see [Brisset et al. \(2018\)](#); [Gejadze & Malaterre \(2017\)](#); [Oubanas](#)  
121 [et al. \(2018\)](#); [Larnier et al. \(2020\)](#); [Garambois et al. \(2020\)](#); [Pujol et al. \(2020\)](#); [Malou et al. \(2021\)](#); [Gejadze et al.](#)  
122 [\(2022\)](#) and references therein. A key aspect of these approaches, well-suited for inferring large parameter vectors  
123 from heterogeneous data, is starting iterative estimation algorithms with sufficiently accurate initial values. Recent  
124 methods define these initial values using probabilistic priors ([Gejadze et al., 2022](#)) (potentially learned from the  
125 datasets) or Machine Learning ([Larnier & Monnier, 2023](#)). However, these sophisticated strategies face bias issues  
126 when dealing with real, imperfect SWOT and/or multi-satellite water surface (WS) observations and uncertain  
127 discharge, bathymetry, and friction. Moreover, these reach-scale discharge estimation approaches may not ensure  
128 coherence in inferred discharge patterns across the river network. Therefore, in the context of discharge inversion  
129 from satellite data, a basin-scale hydrological-hydraulic modeling approach offers two key advantages: (i) Spatial  
130 and temporal coherence of hydrological states and fluxes at the basin scale. (ii) Crucial closure for resolving the  
131 ill-posed discharge inverse problem using WS observables and a hydraulic model.

132

133 The increased spatio-temporal density of WSE measurements brought by SWOT, and the visibility of flow lines  
134 offer new possibilities to estimate spatio-temporal hydraulic parameters. However, satellite altimetry measurements  
135 of WS are relatively sparse in time compared to local flow dynamics. This important aspect of the inverse problem  
136 is investigated in [Brisset et al. \(2018\)](#) through identifiability maps comparing available observations and hydraulic  
137 wave propagation in space and time, enabling to determine the inferrable discharge frequencies ([Brisset et al., 2018](#))  
138 or inferable hydrograph time windows ([Larnier et al., 2020](#)) at reach scale, for a long reach with several tributaries  
139 and using synthetic SWOT data in [Pujol et al. \(2020\)](#). Spatial constraints are also essential, given the generally  
140 sparser observation grid compared to the model grid. Spatial regularization are analyzed using synthetic SWOT or  
141 nadir altimetry data of different sparsity in [Garambois et al. \(2020\)](#) using HiVDI algorithm ([Larnier et al., 2020](#)).  
142 Adequate regularizations and spatial scales for parameters must be chosen in the context of spatial equifinality  
143 (e.g. [Garambois et al. \(2020\)](#); [Pujol et al. \(2024\)](#)), where different parameter spatializations can lead to similar  
144 fits to water surface elevation (WSE) data. The application of Variational Data Assimilation (VDA) to a river  
145 network-scale hydraulic model, informed by a hydrological model for flow consistency, would enable maximizing  
146 information extraction from available flow observations and estimating physically meaningful parameters.

147 This study ultimately addresses the following two connected objectives.

- 148 • Closing the hydraulic ill-posed inverse problem of inferring river discharge from water surface (WS) measure-  
149 ments alone. The method builds on the HiVDI algorithm ([Larnier et al., 2020](#); [Larnier & Monnier, 2023](#))  
150 but aims to close the ill-posed inverse problem through a (sequential) coupling with a hydrological model  
151 over a complete network.
- 152 • Improving integrated hydrological-hydraulic (H&H) models of river networks by leveraging the new SWOT  
153 data that provide hydraulic visibility for worldwide rivers at unprecedented spatial coverage and resolution.  
154 However, local measurement errors can be significant in some cases. This is complemented by altimetry and  
155 imagery from other state-of-the-art satellites to build the prior model geometry.

156 The developed approach is built on a proposed automatic pre-processing chain and the hydrodynamic solver and  
157 dedicated VDA algorithm developed in [Larnier et al. \(2020\)](#); [Larnier & Monnier \(2023\)](#), applied to a complete  
158 network. This approach is based on the following ingredients, all applicable to open source data and other basins  
159 worldwide:

- 160 • A pre-processing algorithm for extracting water surface width (WSW) from optical and radar images, and  
161 water surface elevation (WSE) from ICESat2 altimetry, both used to build the a priori river model geometry.
- 162 • A fine analysis and filtering of 1D L2 SWOT river products, using a wavelet-based processing algorithm  
163 based on ([Montazem et al., 2019](#)) with some upgrades.
- 164 • The Saint-Venant hydraulic model posed on a network (open-source computational software [DassFlow1D](#)  
165 [DassFlow \(2023\)](#)) fed with the discharge values obtained from the pre-calibrated MGB hydrological model  
166 ([Collischon et al., 2007](#); [Pontes et al., 2017](#)).

- The VDA formulation developed in (Larnier & Monnier, 2023; Larnier et al., 2020; DassFlow, 2023) for the HiVDI algorithm, here applied to the complete network, enabling to ingest multi-source heterogenous data and to estimate high-dimensional spatio-temporal parameters, here the bathymetry, spatially distributed frictions and the inflow hydrographs of the hydraulic model.

The sequential coupling Hydrology-Hydraulics enables to define a sufficiently accurate first estimation of the flow to next obtain by the VDA process an (unbiased) accurate space-time variations of the uncertain / unknown fields  $Q(x, t), b(x), K(x)$ .

After the data assimilation process are obtained: (i) a coherent state-flow modeling over river network at basin scale, (ii) sufficiently complex hydraulic modeling to fit high resolution observations of rivers surface deformations.

The remainder of this article is as follows: section 2 presents the modeling approach and the inverse algorithm, section 3 presents the studied case and data and processing chain, results and discussions are detailed in section 4, conclusions and perspectives are given in section 5.

## 2 Model and data assimilation algorithm

This section first presents the forward river network model composed of the "differentiable" 1D Saint-Venant hydraulic network model (DassFlow1D) fed with discharges from the semi-distributed hydrological model MGB. It then describes the variational data assimilation algorithm, which utilizes cost gradients computed with the adjoint of the hydraulic model. The forward-inverse approach is schematized in Figure 1.

### 2.1 Hydrological-hydraulic river network model

We consider a 2D river basin domain  $\Omega_{rr}$  where a spatialized hydrologic model  $\mathcal{M}_{rr}$  is applied. This model is here semi-distributed and operates on a mesh composed of topographical sub-basins. Within  $\Omega_{rr}$ , there is a river network sub-domain  $\Omega_{hy}$ , composed of connected segments  $s = 1..N_{seg}$  between upstream points and successive confluences, where a 1D Saint-Venant  $\mathcal{M}_{hy}$  hydraulic model is applied, with inflows being provided by the hydrological model as follows. Subscripts "rr" and "hy" denote rainfall-runoff and hydraulic components respectively.

First, the 1D Saint-Venant hydraulic model for a given river network segment  $s \in \Omega_{hy}$  is expressed using the curvilinear abscissa  $x$  within segment  $s$  and time  $t > 0$  as follows:

$$\mathcal{M}_{hy} : \begin{cases} W \frac{\partial Z}{\partial t} + \frac{\partial Q}{\partial x} & = q_l \\ \frac{\partial Q}{\partial t} + \frac{\partial}{\partial x} \left( \frac{Q^2}{A} \right) & = -gA \left( \frac{\partial Z}{\partial x} - S_f \right) \end{cases} \quad (3)$$

where  $A(x, t)$  is the cross-sectional area of the flow,  $Q(x, t)$  is the volumetric flow rate,  $q_l(x, t)$  is the lateral inflow per unit length,  $g$  is the acceleration due to gravity,  $Z(x, t) = h(x, t) + b(x, t)$  is the water surface elevation with water depth  $h$  and bed elevation  $b$ ,  $S_f(x, t) = \frac{|Q|Q}{K^2 A^2 R_h^{4/3}}$  is the Manning-Strickler friction slope with  $R_h$

198 the hydraulic radius and  $K(x, h) = \alpha(x)h^\beta(x)$  the friction law that is richer than a constant and well-suited for  
 199 effective 1D modeling of complex flows (e.g. [Garambois et al. \(2017, 2020\)](#)).

200 This hydraulic model is fed by the hydrologic model  $\mathcal{M}_{rr}$  through discharge time series at  $N_{in}$  inflow points,  
 201 with  $N_{up}$  upstream and  $N_{lat}$  lateral inflow points of the coupling interface  $\Gamma_{in} = \Gamma_{up} \cup \Gamma_{lat}$ , determined by prepro-  
 202 cessing as explained later.

203 Discharge time series simulated by the hydrological model are imposed at upstream boundaries and as lateral  
 204 mass source terms in the dynamic hydraulic model. This constitutes a weakly coupled hydrological-hydraulic  
 205 model, denoted as  $\mathcal{M} = \mathcal{M}_{hy}(\cdot, \cdot, \cdot; \mathcal{M}_{rr}(\cdot))$ , with:

$$\mathcal{M}_{hy} : (K(s; x), b(s; x), Z_{down}(t); (\mathbf{Q}_{in}, \mathbf{Q}_{lat})(t)) \mapsto (Z, A, Q)(s; x, t) \quad (4)$$

206

$$\mathcal{M}_{rr} : (\mathbf{I}, \mathbf{D}) \mapsto (\mathbf{Q}_{in}, \mathbf{Q}_{lat})(t) \quad (5)$$

207 Where  $K(s, x)$  and  $b(s, x)$  respectively denote the spatially distributed hydraulic friction coefficient and bathymetry,  
 208  $Z_{down}(t)$  is the water level time series imposed by satellite altimetry as downstream boundary condition (BC) .  
 209 Additionally,  $\mathbf{Q}_{in}(t) = Q_{in,1..N_{up}}(t)$  and  $\mathbf{Q}_{lat}(t) = Q_{lat,1..N_{lat}}(t)$  represent the  $N_{in} = N_{up} + N_{lat}$  inflow hydrographs  
 210 used as upstream BC and lateral source term, respectively, in the hydraulic model  $\mathcal{M}_{hy}$  (Eq. 3) and predicted by  
 211 the hydrological model  $\mathcal{M}_{rr}$  taking as inputs  $\mathbf{I}$  and  $\mathbf{D}$  which are atmospheric forcings and basin physical descriptors  
 212 (cf. section 3.2.1). The classical numerical resolution of the hydraulic network model is explained in appendix A.  
 213 The subsequent focus will be on the estimation of its parameters.

## 214 2.2 Variational data assimilation algorithm

215 The estimation of spatially and temporally distributed controls (bathymetry, friction, inflow discharges) of  
 216 the river network hydraulic model is performed from WS observables using the VDA algorithm developed in the  
 217 so-called HiVDI algorithm, see [Larnier et al. \(2020\)](#); [Larnier & Monnier \(2023\)](#). The core principle of this inverse  
 218 method is to minimize the discrepancy between simulation and observations of river network state dynamics by  
 219 adjusting the parameter vector  $\boldsymbol{\theta}$  of the hydrodynamic model (Section 2.1) starting of a background (first guess)  
 220 estimate  $\boldsymbol{\theta}^{(0)}$ . This method is very efficient for optimizing a large and heterogeneous set of hydrodynamic model  
 221 parameters across an entire river network.

### 222 2.2.1 The sought unknown parameter $\boldsymbol{\theta}$

223 The sought parameter is a large dimensional vector composed of spatially distributed parameters of the hy-  
 224 draulic network model: the friction and bathymetry coefficients over the river network and inflow hydrographs at  
 225 inflow points. It is defined as:

$$\boldsymbol{\theta} = \left[ \left( Q_{in,u}^0, \dots, Q_{in,u}^{T_u} \right)_{u=1..N_{BC}} ; \left( b_{1,s}, \dots, b_{N_b(s),s} \right)_{s=1..N_{seg}} ; \left( \alpha_s, \beta_s \right)_{s=1..N_{seg}} \right]^T \quad (6)$$



where  $Q_{in,u}^{t=1..T_u}$  is the upstream discharge hydrograph imposed at  $N_{BC}$  main inflow points (upstream BCs) with  $T_u$  discharge values in time (evenly or unevenly discrete hydrograph). The spatialized bathymetry-friction over the river network is as follows:  $b_{\square}$  (resp.  $\alpha_{\square}$  and  $\beta_{\square}$ ) is the channel bottom elevation (resp. coefficient and exponent of the friction law) with  $N_b(s)$  (resp.  $N_K(s)$ ) being the number of bathymetry points (resp. friction patches).

Note that for this study, with the above definition, friction is assumed to be spatially uniform within each segment of the river network. This assumption implies a lower spatial density of friction control compared to bathymetry ones. This is a reasonable assumption because (i) the friction parameter in the 1D Manning-Strickler parameterization has a rather large meaningful scale, and (ii) radar altimetry data used for calibration are heterogeneous and sparser than model resolution (cf. bathymetry-friction spatial patches in [Garambois et al. \(2020\)](#) and large scale applications of the algorithm with lateral inflows from MGB hydrologic model [Pujol et al. \(2020\)](#); [Malou et al. \(2021\)](#)).

The same hypothesis will be used for a parameter estimation experiment with the denser SWOT data in space and time.

### 2.2.2 Cost function and optimization algorithm

The principle of the VDA algorithm [Monnier \(2021\)](#); [Asch et al. \(2016\)](#); [Larnier et al. \(2020\)](#) is to estimate (discrete) controls of the river network model that minimize the discrepancy between the simulated flow and the available observations. The cost function to be minimized writes:

$$j(\boldsymbol{\theta}) = j_{obs}(\boldsymbol{\theta}) + \gamma j_{reg}(\boldsymbol{\theta}) \quad (7)$$

In this study, flow observations consist in multi-mission altimetric data  $Z^*$  heterogeneous in space and time (cf. [appendix B](#)), and the term  $j_{obs}$  measures the discrepancy between modelled and observed WS elevations over the hydraulic domain  $\Omega_{hy}$ :

$$j_{obs}(\boldsymbol{\theta}) = \frac{1}{2} \|Z(\boldsymbol{\theta}) - Z^*\|_O^2 \quad (8)$$

The weighted Euclidean norm is defined as  $\|x\|_O^2 = x^T O x$ , with  $O$  an a-priori observation covariance operator, here classically a diagonal matrix of constant variance  $\sigma_o$ . (For more details on the introduced covariance operators, we refer to [Larnier et al. \(2020\)](#); [Larnier & Monnier \(2023\)](#)).

Note that  $j(\boldsymbol{\theta})$  depends on the control parameter  $\boldsymbol{\theta}$  through  $Z$  therefore the response of the hydraulic model  $\mathcal{M}_{hy}$  (Eq. 3) inflowed by the hydrological model  $\mathcal{M}_{rr}$ , therefore the (sequentially) coupled hydrological-hydraulic model  $\mathcal{M}$  (see Eq. 4)

The VDA method consists to solve the optimization problem:

$$\hat{\boldsymbol{\theta}} = \underset{\boldsymbol{\theta}}{\operatorname{argmin}} j(\boldsymbol{\theta}) \quad (9)$$

This optimization problem is high-dimensional, say  $O(10^4)$ . It is solved numerically with the iterative L-BFGS algorithm [Bonnans et al. \(2006\)](#) called in [DassFlow \(2023\)](#). In [DassFlow \(2023\)](#), the gradient  $\nabla_{\boldsymbol{\theta}} j(\boldsymbol{\theta})$  is computed using the adjoint model which is derived by Automatic Differentiation (AD) of the forward code using the AD tool

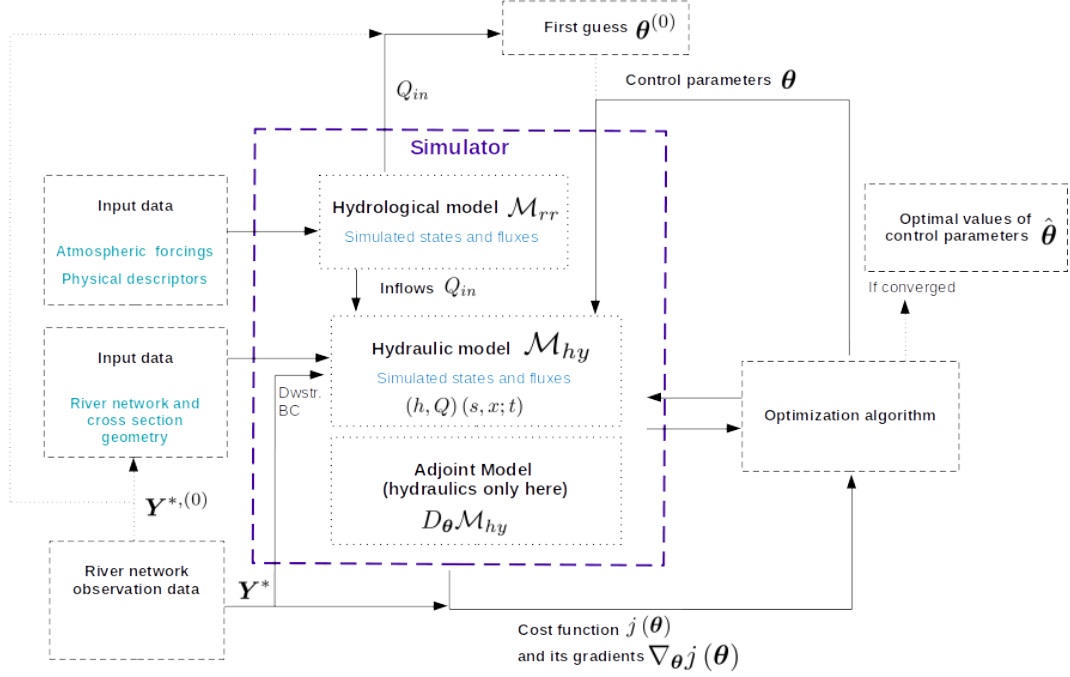


**Figure 1.** Diagram of the adjoint-based variational data assimilation (VDA) algorithm (inspired from principle in Monnier (2021)) applied here to the network scale hydraulic model  $\mathcal{M}_{hy}$  which inflows are provided by the basin scale hydrological model  $\mathcal{M}_{rr}$ .

256 Tapenade Hascoet & Pascual (2013). For further details on the know-hows here implemented, we refer to Monnier  
 257 (2021); Larnier et al. (2020) and e.g. Pujol et al. (2022) for H&H models.

258 The resulting iterative algorithm is schematized in Figure 1. The first guess value (background value)  $\theta^{(0)}$  is  
 259 defined by inverting the hydraulic model in steady state assuming a geometry shape and friction value, given inflows  
 260 provided by a pre-calibrated hydrological model. More details are provided the numerical experiments section.

### 261 3 Data processing chain, studied case and numerical experiment design

262 This sections summarizes the automatic processing algorithms for extracting WSE and WSW from satellite  
 263 data including both drifting (ICESat-2) and non drifting (Sentinel 3), as well as water masks (either optical or  
 264 radar) and SWOT filtering. These algorithms are used in conjunction with a preprocessor for hydraulic model  
 265 meshing and coupling to a precalibrated hydrological model, which is presented next. Finally, the data assimilation  
 266 experiment plan is outlined.

267 This study focuses on the Maroni River basin (MRB), in French Guiana, which experiences a tropical climate  
 268 with distinct rainy and dryer seasons. The study utilizes a diverse and rich dataset (Figure 2) processed with new  
 269 dedicated algorithms before feeding the different components of the forward hydrological-hydraulic model and the  
 270 VDA algorithm as follows:

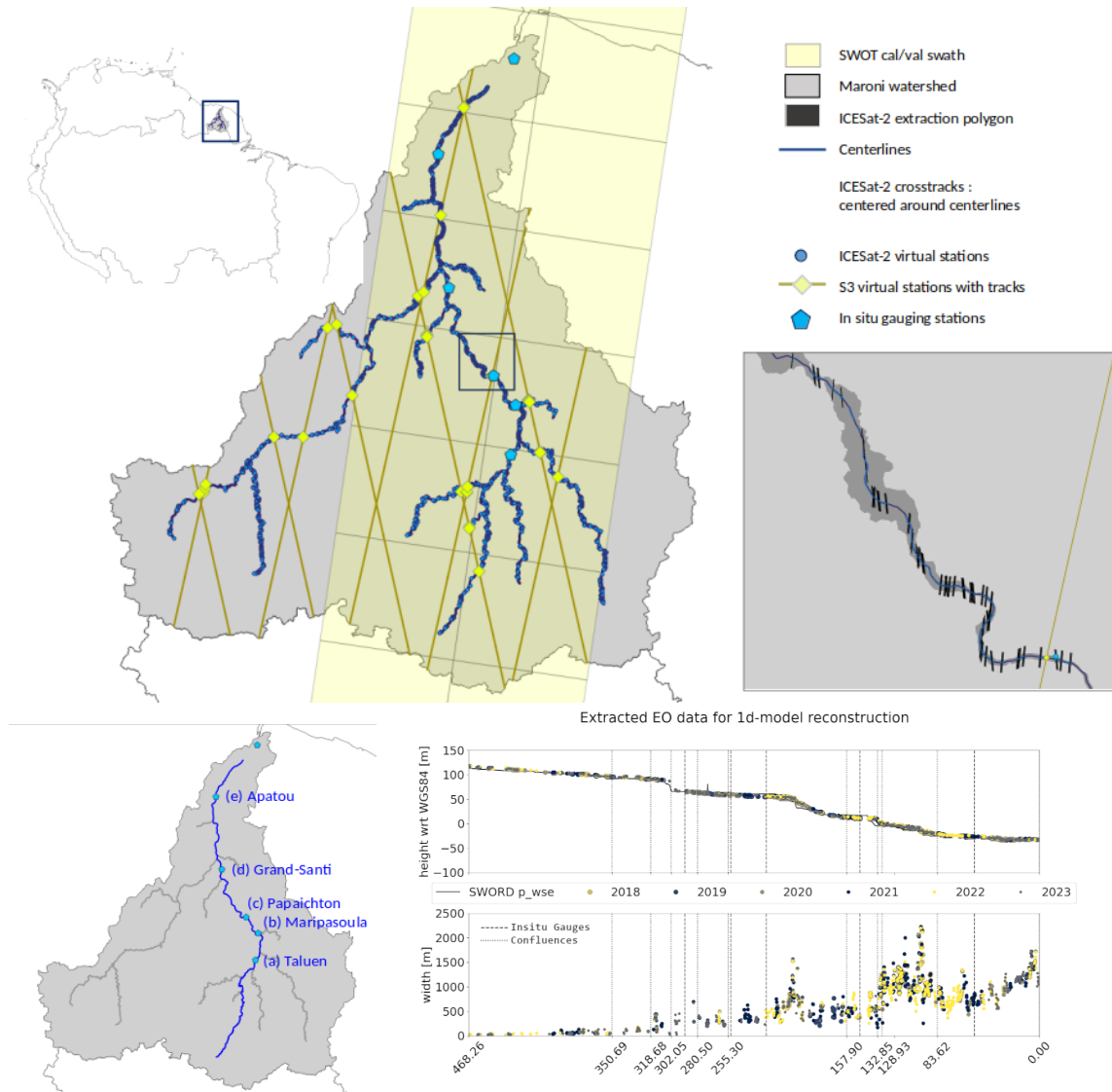


**Figure 2.** The Maroni River basin in French Guiana with (top) multi-satellite and in situ flow observability over the river network for model building and data assimilation, (Bottom) an example of water surface profiles geometry over the Maroni main stream, including elevation data from drifting nadir altimetry (ICESat-2) and width from images (Sentinel 1).

- 271
- 272
- 273
- 274
- 275
- 276
- 277
- 278
- 279
- **Hydrological modeling (MGB) inputs** : physical basin descriptors for semi-distributed mesh of the basin and a priori parameters constrains and hydrometeorological data from worldwide open databases for model setup, discharge at in situ gauges for its calibration (seedetail in subsection 3.2.2).
  - **Hydraulic modeling (DassFlow1D) inputs** : A priori river network database and multi-satellite dataset of WSE (ICESat2) and WSW (Sentinel) profiles for model geometry construction, inflow discharge from the hydrological model for a priori bathymetry estimation (see section 3.2).
  - **Variational Data Assimilation (VDA) inputs:** WSE data from Multi-satellites, Sentinel 3 and ICESat2 for spatial density with in situ georeferenced gauges WSE time series for temporal density, or SWOT alone and.

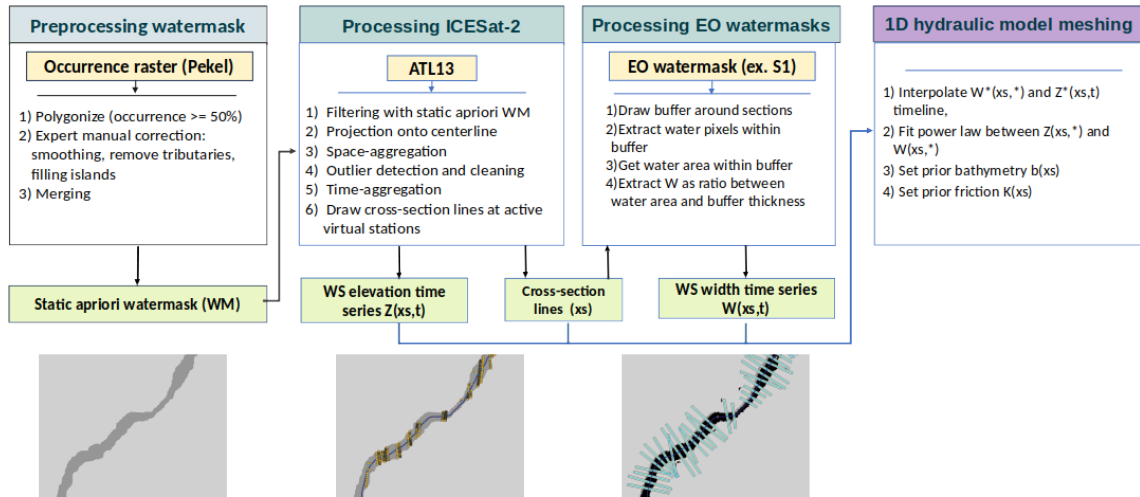


**Figure 3.** Flowchart of the processing chain for water masks derived from satellite images and ICESat2 altimetry data  $Z^*$ , including 1D hydraulic model meshing using cross-sections computed with  $W^*$  interpolated on the  $Z^*$  timeline.

### 3.1 Water surface elevation and width processing from altimetry and radar images

Water surface elevation (WSE) data are derived from processed Sentinel 3 data at virtual station (VS) and drifting ICESat-2 ATL13 data using a proposed processing chain. This chain utilizes an a priori water mask and aims to provide hydraulically consistent WSE on cross-section (XS) lines over the river network shapefile (Figure 3, appendix D).

Water surface width (WSW) data are extracted from dynamic water masks using the ExtractEO tool from ICube-SERTIT applied to derive relatively high resolution water masks from Sentinel-1 radar images (cf. Appendix E). These widths (cf. statistics in Figure 4) are used for XS parameterization later. Sentinel data, relatively accurate, is chosen for WSW to enhance information extraction from SWOT WSE data that will be used alone in assimilation.

SWOT data offers remarkable hydraulic visibility but contains measurement errors. We use the SWOT L2 RiverSP product for WSE along river centerlines at a 200m resolution, applying a wavelet-based filtering and segmentation algorithm following Montazem et al. (2019) (Appendix F)). The filtering of SWOT 1-day orbit data is presented in Figure 5, efficiently removes main outliers while depicting multiscale hydraulic information.

The WSE data, whether from altimetry or in situ measurements, are in the same WGS84 vertical reference frame. The observation dataset  $\mathbf{Y}^{*,(0)}$ , for determining the prior mesh cross-section geometry of the hydraulic model, consists of IceSat2 WSE  $Z^*$  and Sentinel width  $W^*$  on the 2020 period. Three independent assimilation subsets  $\mathbf{Y}^*$ , covering distinct time periods in 2019 or 2023, are composed of altimetry data WSE  $Z^*$  from Sentinel and in situ heights, or SWOT data only (Appendix A).

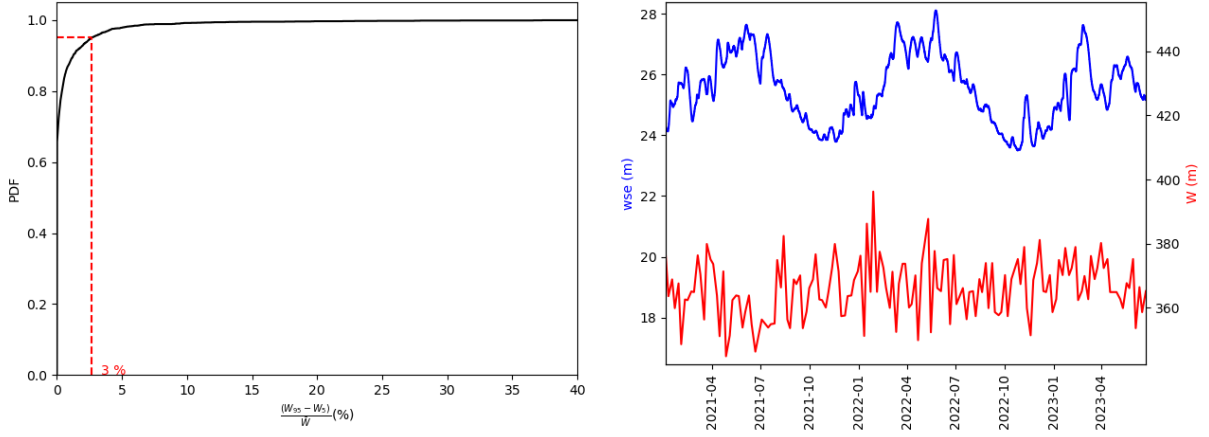


**Figure 4.** Width variability. (Left) Cumulative distributions of relative width variability computed using using the 95-th and 5-th centiles (in order to filter potential noisy extremums), over the whole hydraulic network  $\Omega_{hy}$  and 2021-01 to 2023-05 period of temporal water masks, for each cross-section width data are previously filtered to ensure a monotonic increasing relation  $W(H)$ . 95% of the sections exhibit temporal relative variability lower than 3%. (Right) An example from the Papaichton gauging station illustrates the variability of  $W$  and  $H$ . The timeseries of  $H$  and  $W$  show no evident correlation, suggesting that the variability in width measurements stems from uncertainties in the computation derived from water masks.

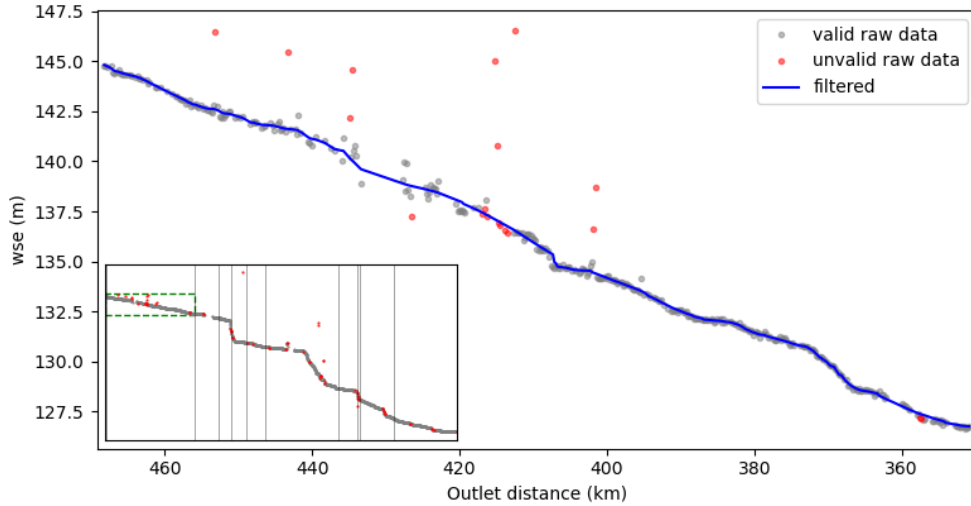


**Figure 5.** Hydraulic filtering of SWOT L2-RiverSP products at node scale on the main stem for cycle 569 using the pyrswt algorithm (Python River Segmentation with Continuous Wavelet Transform). The main plot focuses on the first upstream segment of the main stem, displaying the filtered profile as a solid blue line. The inset plot presents the complete main stem, with a dashed green rectangle indicating the zoom area of the main plot, and vertical gray lines marking the segment boundaries, which correspond to main confluences.

## 3.2 Maroni H&H model construction

### 3.2.1 Hydrological model setup

The hydrological model  $\mathcal{M}_{rr}$  used is the MGB semi-distributed model well-suited for this tropical basin. Classical preprocessing was applied to obtain flow directions and accumulations based on MERIT-Hydro DEM (Yamazaki et al. (2019)), following the steps outlined in Pontes et al. (2017). Spatial hydrological response unit (HRU) descriptors on soil and vegetation were derived from FAO HWSO (Nachtergaele et al. (2023)) and ESA WorldCover (Zanaga et al. (2021)), respectively, and converted into 12 HRUs with distinct flow-generation potential. Hydro-meteorological forcings, including climate and rainfall data, were obtained from ECMWF ERA5 dataset and GSMAP-RT real-time product (Kubota et al. (2020)). The MGB model is manually calibrated using in situ discharge data with low parameters spatialization. The Maroni River basin is divided into 10 sub-basins corresponding to the main tributaries: the Litani, Tampok, Grand Inini, Lawa, Gonini, Upper Tapanahoni, Palumeu, Tapanahoni, Abounami and Maroni. Calibration is performed using observed discharge data from SCHAPI's <https://www.hydro.eaufrance.fr/> (accessed on 2024-05-25) at 5 gauging stations: Lawa at Taluen, Tampok at Degrad-Roche, Lawa at Maripasoula, Maroni at Grand-Santi and Maroni at Langa-Tabiki (see Figure 2). The calibration period spans from 2016 to 2023. Calibration is simply performed sequentially from upstream to downstream, considering uniform parameters for each large calibration basin. Ungauged basins are calibrated using the nearest downstream gauge. The discharge simulated, at a daily time step, by the semi-distributed hydrological model are used to feed the hydraulic model at its upstream and lateral inflow boundaries defined below.

### 3.2.2 Hydraulic mesh and coupling with hydrology

An automatic pre-processing algorithm designed to build coupled hydrological-hydraulic model setup for MGB and DassFlow1D is fed by the multi-satellite data preprocessing chain presented in section 3.1.

The hydraulic domain  $\Omega_{hy}$  is determined using the river centerlines from SWORD database Altenau et al. (2021). The downstream boundary is set at Apatou, at a point disconnected from tidal influence because of a sharp river channel bottom variation. Upstream limits are set for rivers draining more than  $1500\text{km}^2$ , based on drainage area obtained from DEM processing. Thus, the hydraulic model covers a long portion of the Maroni main course and many of its tributaries.

Once the hydraulic river network domain  $\Omega_{hy}$  is determined, the upstream inflow points can be readily identified. In this case, there are  $N_{BC} = 12$  such points, where the discharge from the hydrological model serves as boundary conditions for the 1D hydraulic model resolution. Additionally, lateral inflow points are determined, with  $N_{lat} = 181$  points identified. Upstream and lateral inflows represent 36% and 50% of the hydrological drainage area respectively. The remaining 14% mainstream subcatchments were ignored to simplify the coupling process, given other uncertainties and the corrections of mass inflows and dynamics that will be addressed through assimilation. The hydraulic mesh and coupling points are depicted in Figure 6.

The hydraulic network model  $\mathcal{M}_{hy}$  is driven by inflow discharge hydrographs, provided by the pre-calibrated hydrological model  $\mathcal{M}_{hy}$ . These hydrographs, used as background in data assimilation after, are and denoted  $Q_{in,i=1..N_{BC}}^{(0)}(t)$  for upstream inflows and  $q_{lat,i=1..N_{lat}}^{(0)}(t)$  for lateral inflows.

### 3.2.3 Hydraulic model geometry

The a priori geometry of the hydraulic model across the river network is automatically determined from a multi-satellite dataset not used in DA experiments: a median water mask  $W^{*,50}$  (Sentinel 1 processed with ExtractEO) and a median flow line  $Z^{*,50}$  (ICESat2 WSE profiles, cf. section 3.1), over the period 2019-2021.

In this work, the XS geometry shape of the hydraulic model is defined as rectangular using the median water mask  $W^{*,50}$ , which is a reasonable assumption, given the relatively limited extent temporal variations observed across the entire river network, as shown in Figure 4, and considering the uncertainty in water masks. Furthermore, this rectangular XS shape hypothesis has been successfully applied to the "nearby" anastomosed Negro River in our previous studies (Pujol et al., 2020; Malou et al., 2021). It is important to note that the width of this rectangular cross-section is spatially variable, thereby defining prismatic channels. This variability, combined with the optimized spatially distributed bottom elevation and friction parameters, enables the simulation of complex hydraulic controls and their associated nonlinear signatures on the water surface profile as shown after. This ultimately results in a good fit to altimetry data and satisfactory discharge inference.

Following the strategy developed in Larnier et al. (2020) (HiVDI algorithm for a single river portion), the background (first guess value) river bed elevation  $b_{x,s}^{(0)}$  is obtained by inverting a system based on the Low Froude flow model (Eq. 2) at river network scale using: constant friction  $K^{(0)} = 30 \text{ m}^{1/3} \cdot \text{s}^{-1}$  (an arbitrary "mild" value for large rivers), a median flow line  $Z^{*,50}$  from ICESat2 WSE, and the discharge  $Q$  and WS slope  $S$  from a steady state forward run of the hydraulic network model fed by median hydrographs (on the corresponding period) of the hydrological model at upstream and lateral inflow points.

This relatively straightforward method enables the determination of a non-trivial bathymetry background  $\mathbf{b}^{(0)}(x, s)$  with realistic spatial variability across a river network, using WS observations. This approach is applicable where altimetry data are available, such as spatially dense cross-sections from ICESat-2 here. Figure 6 illustrates this on the main stream of the Maroni River, displaying the mesh granularity, cross-section width, and bottom elevation variations, including a succession of marked riffles and jumps corresponding to hard rock outcrops. This is one of the river portions over which 1-day orbit SWOT data will be integrated.

Using this background on bathymetry-friction-inflow discharge

$$\boldsymbol{\theta}^{(0)} = (Q_{in,u=1..N_{BC}}^{(0),t=1..T_u}, \mathbf{b}_{x,s}^{(0)}, \alpha_s^{(0)} := 30, \beta_s^{(0)} := 0) \quad (10)$$

which is physical meaningful since it respects the Low-Froude model, the VDA algorithm will seek optimal parameter sets  $\hat{\boldsymbol{\theta}}$  of the dynamic hydraulic model, according to the cost function used.



Note that our modeling chain supports the use of more complex geometries, including, a rectangle for wet bathymetry and a superimposition of trapeziums from dynamic water masks (cf. Larnier et al. (2020)). Our algorithm facilitates this complexity, and future research will explore this capability further, with wet bathymetry parameterizations from S. L. Dingman (2007); S. L. Dingman & Afshari (2018) as applied at reach scale in Andreadis et al. (2020).

### 3.3 Numerical experiments design

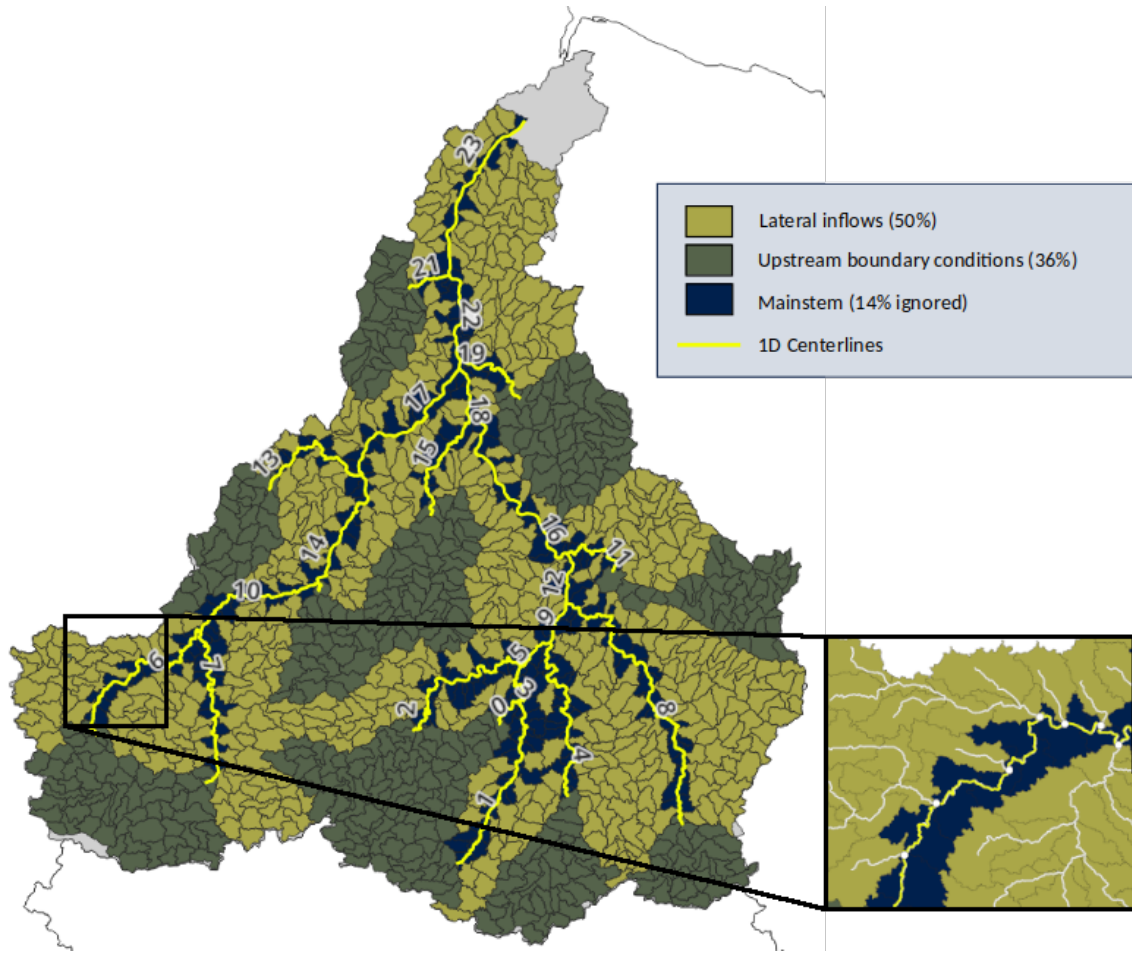
The Multi-satellite data assimilation experiments utilize the VDA algorithm applied to the coupled hydrological-hydraulic model  $\mathcal{M}$  (see section 2). These experiments aim to demonstrate the potential for simultaneously estimating inflow discharges, bathymetry and friction parameters of the hydraulic model at river network scale from WSE data only, which presents a significant challenge. Validation of all experiments considers two key aspects:

- **Fit Improvement:** The enhancement in fit to WSE compared to the assimilated dataset in each case.
- **Discharge Time Series:** Analysis of discharge time series simulated at internal gauges, which are never assimilated, nor are stage-discharge laws which are implicitly optimized at network scale in the assimilation process via bathymetry and friction fields.

The sought parameter vector  $\theta$  of the hydraulic model  $\mathcal{M}_{hy}$  is composed of  $Q_{in,u=1..N_{BC}}^{t=1..T_u}$  hydrographs at  $N_{BC} = 12$  inflows, bathymetry  $b$  at  $N_b = 2572$  points and friction coefficients  $\alpha$  and  $\beta$  at  $N_K = 24$  friction patches (i.e. spatially uniform segments). For each DA experiment, the same median WS width  $W^*$  is used to define cross-section geometry over the river network. However, the first guess on bathymetry  $b^{(0)}$  varies, as it is computed for different periods using different median inflow discharges and median altimetric flow lines  $Z^*,50$ , following the previously explained method. The numerical experiment plan, which involves assimilating various combinations of water surface altimetry data to infer the previously defined hydraulic parameter vector  $\theta$ , is as follows:

1. **"N4I.2019"**: Nadir altimetry, drifting IceSat2 and fixed S3 VS, plus 4 in situ WS elevation time series at Maripasoula, Papaïchton, Grand Santi and Apatou gauges (with a WGS84 vertical reference in coherence with altimetry), over the period 2019/01/01 - 2019/03/31; (hence  $b$  is optimized at those in situ gauges locations);  $T_u = 90$  and prior bathymetry is  $b_{N4I.2019}^{(0)}$ .
2. **"N4I.CalVal"**: Nadir altimetry, drifting IceSat2 and fixed S3 VS, plus 4 in situ WS elevation time series at Maripasoula, Papaïchton, Grand Santi and Apatou gauges (with a WGS84 vertical reference in coherence with altimetry), over the period 2023/05/15 to 2023/07/10; (hence  $b$  is optimized at those in situ gauges locations);  $T_u = 100$  and prior bathymetry is  $b_{N4I}^{(0)}$ .
3. **"SWOT.CalVal"**: 1-day SWOT orbit data only assimilated over the period 2023/05/15 to 2023/07/10. They cover a large part of the modeled Maroni river network as shown in Figure 2, which enables evaluating SWOT potential for correcting a river network model.  $T_u = 100$  and prior bathymetry is  $b_{N4I}^{(0)}$ .





Model 1d geomorphology over main stem

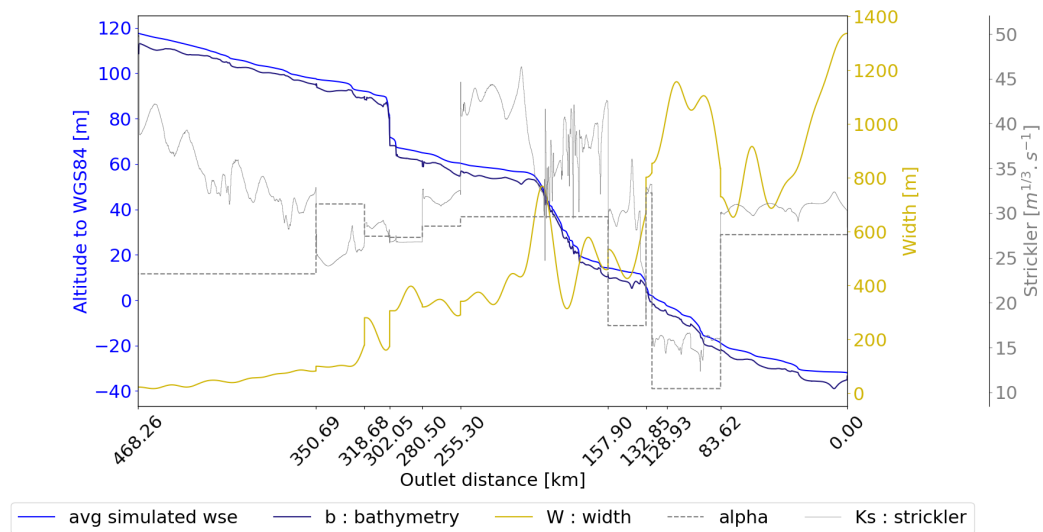


**Figure 6.** Hydrological-hydraulic mesh with inflow points, percentage of hydrological drainage area given in parenthesis (Top). Simulated flow line profile on the Maroni main stem after assimilation of SWOT 1 day data (VDA experiment "SWOT only"), calibrated bathymetry, and friction profiles  $\hat{b}(s, x)$  and  $\hat{K}(s, x, \bar{h}) = \hat{\alpha} \bar{h}^{\hat{\beta}}(s, x)$  (grey Strickler axis for  $\alpha$  values, note the different unit) for successive connected segments  $s = (1, 3, 5, 9, 12, 16, 18, 22, 23)$  (delimited by main confluences with given abscissas) with  $\bar{h}(s, x)$  the average flow line on the studied SWOT time window (Bottom).

Note that using in situ WSE time series in "N4l" configurations provides temporally dense information, supplementing the sparser IceSat-2 and Sentinel-3 data. However, it does not provide explicit information on the stage-discharge relationship, which is implicitly sought for the whole river network during assimilation.

The SWOT CalVal period in 2023 for the second and third experiments, which will be compared, coincides with the end of the rising limb and the recession of a strong flood. In contrast, the first experiment, conducted in 2019, is characterized by a weaker discharge and a "less dynamic" scenario. Therefore, a model warm-up strategy will be employed for the second and third experiments. This strategy involves running the forward hydrological-hydraulic model before assimilation to ensure more realistic flow propagation dynamics in the river network, starting the Variational Data Assimilation (VDA) just at the end of a rising limb.

These VDA experiments, initiated from the prior  $\theta^{(0)} = (Q_{in,u=1..N_{BC}}^{(0),t=1..T_u}, \mathbf{b}_{x,s}^{(0)}, \alpha_s^{(0)} := 30, \beta_s^{(0)} := 0)$  with inflows derived from the MGB hydrological model, aim to investigate the constraining power of classical nadir or wide swath SWOT altimetry. The goal is to constrain a hydraulic model of a poorly gauged basin built from remote sensing data. Particular attention will be given to the potential for estimating spatialized channel parameters and inflow hydrographs.

Note that all these inference scenarios correspond to a quasi-ungauged setup for the inversions over the hydraulic network. This means that in situ discharge information within the studied hydraulic domain  $\Omega_{hy}$  is not considered in assimilation, except indirectly at its boundaries via the inflow discharge from the hydrological model. Specifically, discharge data at in situ gauges were used only for the pre-calibration of the hydrological model. This model provides a priori hydrographs at inflow BCs, and the median discharge in time is used to determine a priori hydraulic bathymetry. In situ discharge time series, which are not assimilated, will be used for analyzing performance after assimilation of water surface elevations.

For every experiment, the parameters of the background error covariance matrix  $B$ , used in the VDA algorithm and influencing the optimal solution  $\hat{\theta}$ , are set a priori from physical considerations as investigated in [Larnier et al. \(2020\)](#); [Garambois et al. \(2020\)](#); [Pujol et al. \(2020\)](#). The parameters  $L_Q$  and  $L_b$  act as correlation length in space and time, respectively, while the  $\sigma_{\square}$  may be viewed as variances. Given the typical low Froude number of the flows at the observation scale and hydrological frequencies for this large basin, adequate values for these parameters are:  $(\sigma_{Q_{in,i}} = 0.01\bar{Q}_{in,i}^{(0)})_{i=1,N_{BC}}, L_Q = 10days, \sigma_b = 0.1m, L_b = 200m, \sigma_{\alpha} = 0.5m^{1/3}.s^{-1}$  and  $\sigma_{\beta} = 0.01$ .

The solvability of the inverse problem (9) obviously depends on the available data, their nature, and their space-time density versus the nature and dimension of the inferred parameter  $\theta$ . On the concept of identifiability in the present hydraulics context, we refer to [Brisset et al. \(2018\)](#), which highlights key concepts that roughly enable understanding the solvability of the treated inverse problem or not and the inferrable hydrograph frequencies. In the present multi-physics network configuration, we have decided to first focus on the identifiability of the upstream inflows of the hydraulic network model, without considering the lateral ones (the latter being given by the hydrological model). [Pujol et al. \(2020\)](#) shows that the simultaneous inference of lateral inflows and channel

432 parameters can be done, however it was on a single (long) reach. Adding the lateral inflows to the uncertain  
 433 parameters (in the vector  $\theta$ ) using the considered dataset and the present H&H model in addition to the bathymetry  
 434 and friction parameters over a river network, should be investigated in a future study.

## 435 4 Results and discussions

436 The overall performances, both in terms of fit to the WSE data used in calibration (either nadir altimetry and  
 437 in situ WSE for N4l, or SWOT data alone) and the reproduction of discharge at gauging stations within hydraulic  
 438 domain  $\Omega_{hy}$  (not used in assimilation), is very satisfactory for the three VDA experiments (Figure 7). Notably,  
 439 there is a very significant improvement in the fit to observed WSE over the spatio-temporal domain, with errors  
 440 reduced to below 0.5m. This improvement of the simulated WSE profiles, in terms of relative cost improvement  
 441  $\left[ J(\theta_{\square}^{(0)}) - J(\hat{\theta}_{\square}) \right] / J(\theta_{\square}^{(0)})$  is of 95% for "N4l.2019", 93% for "N4l.CalVal" and of 86% for "SWOT.CalVal", which  
 442 has a much denser dataset.

443 The performance in terms of simulated discharges at validation gauges (discharge is not assimilated, only WSE  
 444 in N4l configuration) within the river network is also very satisfactory with significant improvements from prior  
 445  $\theta_{\square}^{(0)}$  to inferred  $\hat{\theta}_{\square}$  model parameters. The NRMSE improvements from the prior range from:

- 446 • 32% to 76% for "N4l.2019" (with values in 0.09 to 0.23).
- 447 • 29% to 71% for "N4l.CalVal" (with values from 0.06 to 0.22) and from 18% to 71% for "SWOT.CalVal"  
 448 (with values from 0.05 to 0.18).

449 These improvements, both in fitting the assimilated WSE and in predicting unseen discharge timeseries at internal  
 450 gauges for two distinct time periods with different hydrological responses, validate the method. This is achieved by  
 451 simultaneously optimizing bathymetry, friction across the entire river network, and upstream inflow hydrographs  
 452 from WSE only. Notably, WSE time series at gauges are not assimilated in "SWOT.CalVal" which is compared to  
 453 "N4l.CalVal". A detailed analysis of the results from the three data assimilation (DA) experiments is provided after.  
 454 The analysis covers the fit to the assimilated *WSE* observations, validation against in situ discharge timeseries at  
 455 gauges, and correction of the hydraulic parameters.

### 456 4.1 Multimission nadir altimetry and in situ WSE assimilation 2019 (N4l.2019)

457 This analysis focuses on the assimilation experiment "N4l.2019", which integrates S3 and ICESat2 nadir  
 458 altimetry data along with in situ WSE at the four in situ gauges.

459 Figure 7 presents the minimization of the cost function and its gradients to the sought spatialized parameters,  
 460 along with the fit to WSE data of the model before  $\mathcal{M}(\theta_{N4l}^{(0)})$  and after  $\mathcal{M}(\hat{\theta})$  calibration. The fit of WSE is  
 461 significantly improved from the background prior parameters  $\theta_{N4l}^{(0)}$  to the control  $\hat{\theta}$  estimated by VDA of WSE. The  
 462 simulation error on WSE is within [-0.5, 0.5]m for 88% of the data points, and within [-0.25, 0.25]m for 69% of the  
 463 data points. The 5 - th and 95 - th percentiles of the errors are  $\epsilon_{Q5} = -0.6$ m and  $\epsilon_{Q95} = 0.53$ m, respectively.

This represents a significant improvement in the fit to the spatio-temporally heterogeneous WSE data used in calibration. Interestingly, this also results in a significant improvement in the simulated discharge at the gauging stations within the hydraulic domain  $\Omega_{hy}$ , as evidenced by Figure 4.1 (final NRMSE between 0.08 and 0.19). It is important to note that discharge data were not used in this calibration; only WSE data from four out of five gauges were used, with gauge section bathymetry and friction inferred.

The data assimilated in "N4I.2019" consist in relatively sparse WSE over the spatio-temporal domain (284 satellite altimetry points over the network) with some temporal density provided by WSE at the four gauges (2,161 WSE values per gauge, totaling 8,644). This is compared to the size of the sought spatio-temporal controls. Internal discharge prediction is improved after assimilation of WSE, compared to the prior hydraulic model, at all gauges which are located along the Maroni main stream. This improvement results from the correction of hydraulic model controls which pertain to spatialized channel bathymetry-friction and hydrographs at  $N_{BC} = 12$  upstream inflow points.

Those satellite-based estimates of mass fluxes and river network bathymetry-friction parameters  $\hat{\theta}_{N4I}$ , at the upstream boundaries  $\Gamma_{up}$  and over the river network hydraulic domain  $\Omega_{hy}$  are summarized in Figure 9. Significant corrections of bathymetry-friction are obtained for most segments of the river network. These corrections, along with adjustments of upstream inflow corrections (see inferred inflows hydrographs and bathymetry profiles in appendix G), improve the fit of the simulated flow line to local altimetry and in situ WSE data. Several factors contribute to the complexity of the influence of these hydraulic parameters on the simulated flow line through the hydraulic model :

- **Upstream to downstream propagation:** the inflow discharge propagates and aggregates along the river network. Only upstream BCs on  $\Gamma_{up}$ , representing 50% of basin area as shown by Figure 6), are corrected here.
- **Local competition between bathymetry and friction:** These parameters are embedded in the friction source term  $S_f$  of the 1D Saint-Venant (Equation 3).
- **Downstream controls:** complex correlated influence of the sought hydraulic controls towards upstream on so called backwater length under the fluvial regime studied (see Samuels (1989); Montazem et al. (2019))

In essence, the inverse problem of estimating most flow controls (except lateral inflows) of the network Saint-Venant model is challenging due to local equifinality and spatial equifinality. A satisfying solution was achieved thanks to a realistic prior on the sought parameters and the regularizations introduced via covariances matrices (cf. section 2.2.2). A more detailed hydraulic analysis of the inferred local hydraulic controls, along with discussion on the controllability of hydrological inflows, is made after.

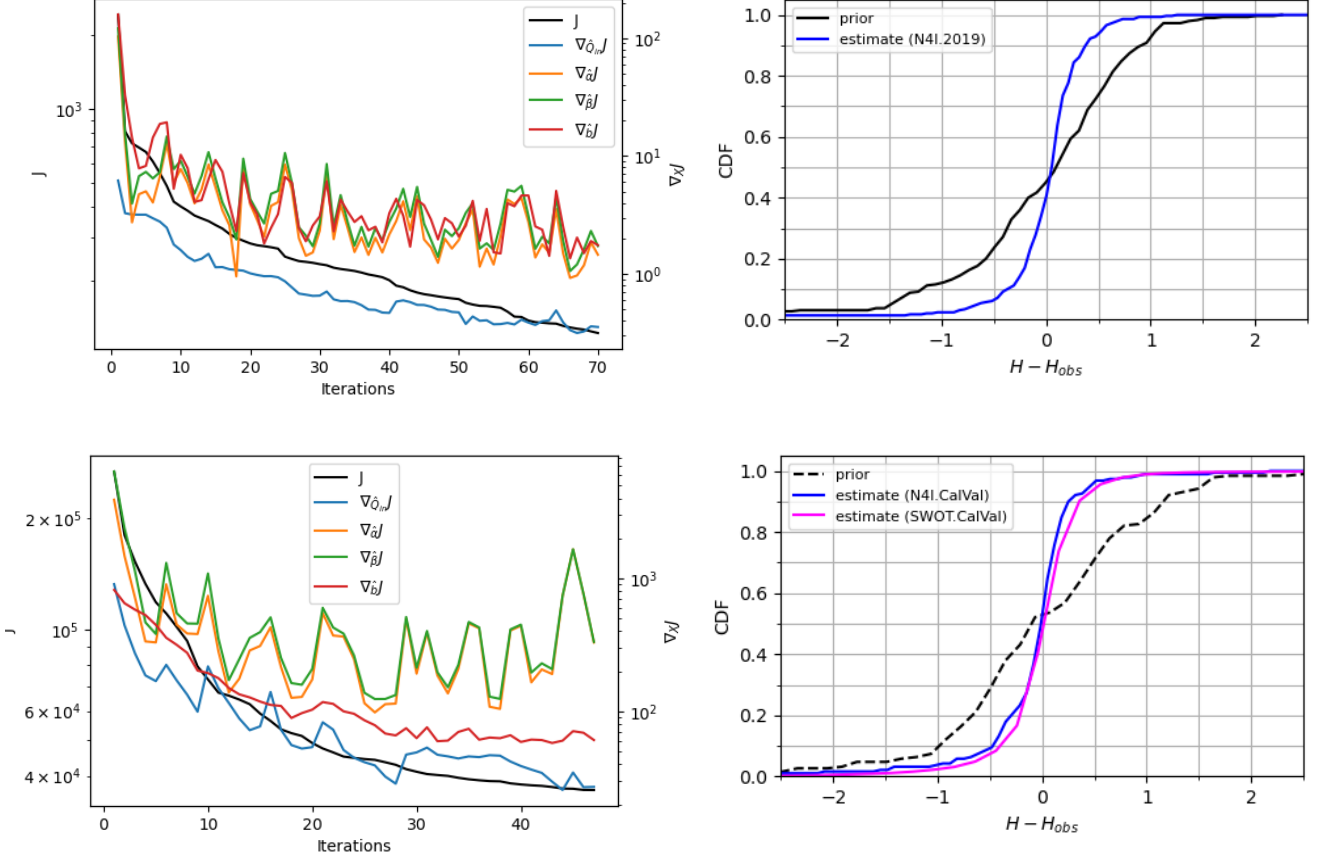


**Figure 7.** (Left) Convergence curves of cost  $J$  (Eq. 7) and evolution of its gradients  $\nabla_{\square}$  with respect to the sought spatio-temporal parameters. (Right) cumulative distribution function (CDF) of absolute misfit of simulated WSE to altimetry data which are assimilated in meters for "prior" (background)  $\hat{\theta}^{(0)}$  and calibrated parameters  $\hat{\theta}_{\square}$ . Model misfit values are as follows: (Top) "N4I.2019" (8,928 space time points from nadir altimetry and in situ WSE) 88% in  $[-0.5, 0.5]$ m, 69% in  $[-0.25, 0.25]$ m, the 5 - th and 95 - th percentiles of errors are  $\epsilon_{Q5} = -0.6$ m, (resp.  $\epsilon_{Q95} = 0.53$ m), respectively; (Bottom) "NAl.CalVal" (5,467 space time points from nadir altimetry and in situ WSE), 87% in  $[-0.5, 0.5]$ m, 68% in  $[-0.25, 0.25]$ m, the 5 - th and 95 - th percentiles of errors are  $\epsilon_{Q5} = -0.9$ m and  $\epsilon_{Q95} = 0.45$ m, respectively; and "SWOT.CalVal" (179,192 space time points from SWOT only), 88% in  $[-0.5, 0.5]$ m, 68% in  $[-0.25, 0.25]$ m, the 5 - th and 95 - th percentiles of errors are  $\epsilon_{Q5} = -0.6$ m and  $\epsilon_{Q95} = 0.52$ m, respectively.

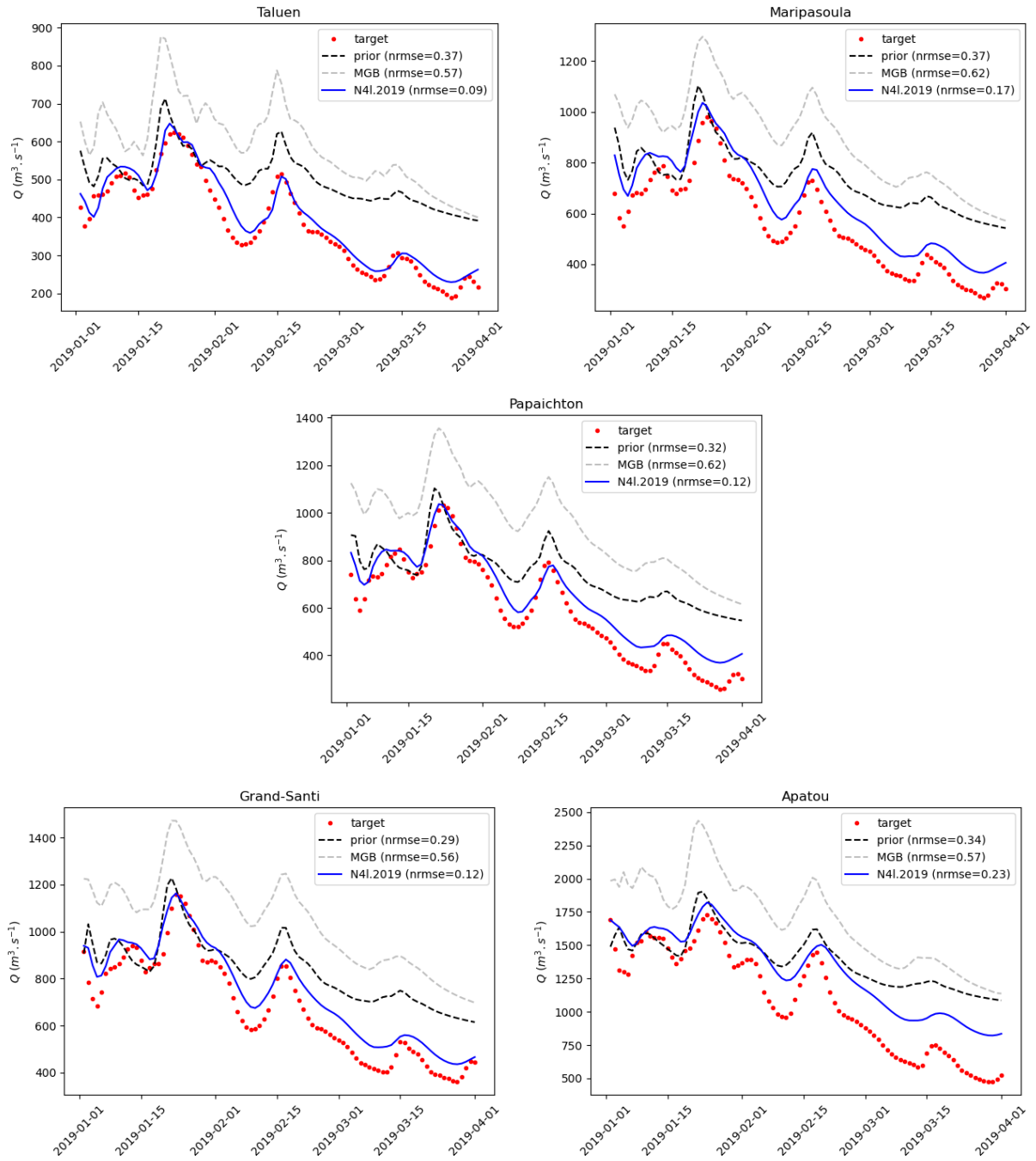


**Figure 8.** Validation of the calibrated Saint-Venant river network model on 2019 period: simulated discharge at internal gauges along the Maroni main stream following the assimilation of nadir altimetry (Sentinel 3 and ICESat-2) and in situ WSE at (excluding Taluen) in the "N4I.2019" experiment. The nRMSE ranges from 0.09 for the Taluen station to 0.23 for the Apatou (most downstream) station.

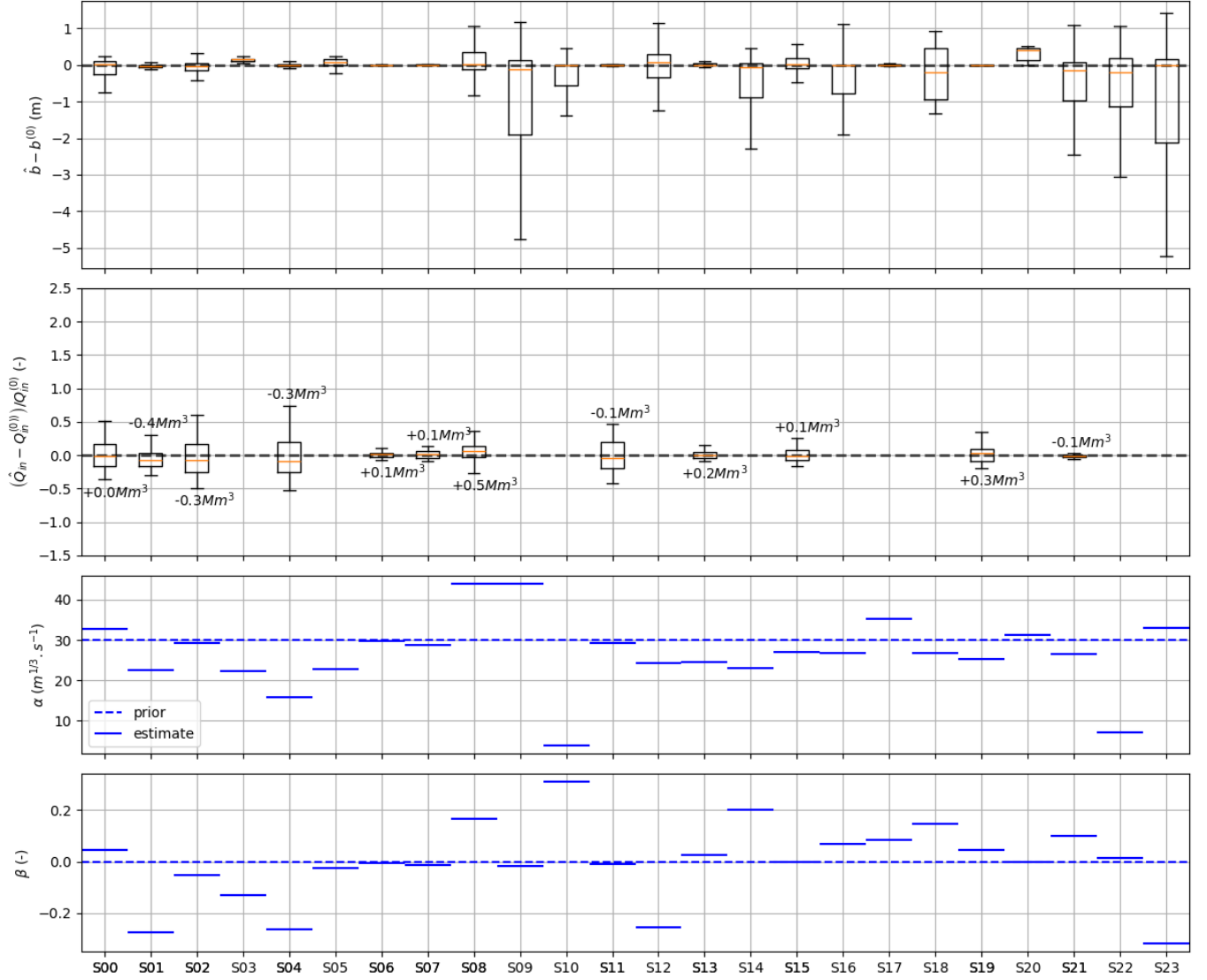


**Figure 9.** Relative correction of hydraulic model parameters after assimilation of nadir altimetry and in situ WSE data in the experiment "N4l.2019". The figure shows inferred parameters  $\hat{\theta}$  by VDA from the background  $\theta_{N4l}^{(0)}$ , represented by river network segment "S00" to "S23". (Top) boxplots of spatially distributed corrections of bathymetry  $b(s, x)$  at  $N_b = 2,572$  hydraulic cross sections and of (second) inflow discharge hydrographs  $Q_{in,u=1..N_{BC}}^{t=1..T_u}$  at  $N_{BC} = 12$  inflows, (third and fourth) friction parameters  $\hat{\alpha}$  and  $\hat{\beta}$  across the 24 segments composing the simulated river network.



## 4.2 SWOT CalVal 1-day orbit (SWOT.CalVal and N4l.CalVal)

This analysis focuses on the assimilation experiment of "SWOT.CalVal", which utilizes wide swath altimetry data from track #007 during fast sampling (cal-val) orbit. This data covers a large area of the Maroni basin, including the main stream "along track" with a 1 day repeat cycle. The results of the "SWOT.CalVal" experiment are compared with the "N4l.CalVal" experiment, which assimilates S3 and ICESat2 nadir altimetry data along with in situ WSE data over the same time period.

The time period from 2023-05-15 (start of consolidated SWOT measurements) to 2023-07-10, covered by SWOT's 1 day orbit data, corresponds to the peak and declining limb of a relatively strong flood: the estimated peak flow in May 2023 at Apatou downstream of the basin is above 4,500 m<sup>3</sup>/s. Therefore, a warm up period is used to obtain a physically meaningful initial state in the river network for starting assimilation (cf. details in section 3.3). Note that a wavelet-based filtering algorithm is systematically applied to remove outliers in SWOT data (cf. Figure 5) before VDA.

Figure 7 presents the minimization of the cost function and its gradients to the sought spatialized parameters, along with the fit to SWOT WSE data of the model before  $\mathcal{M}(\theta_{SWOT}^{(0)})$  and after  $\mathcal{M}(\hat{\theta})$  calibration. The fit of WSE is significantly improved from background prior parameters  $\theta_{SWOT}^{(0)}$  or  $\theta_{N4l}^{(0)}$  to the control  $\hat{\theta}$  estimated by VDA of WSE respectively for SWOT or nadir and in situ.

For "SWOT.CalVal", the simulation error on WSE is within [-0.5, 0.5]m for 88% of the data points, within [-0.25, 0.25]m for 68% of the data points. The errors for the 5 - th and 95 - th percentiles are  $\epsilon_{Q5} = -0.6$ m and  $\epsilon_{Q95} = 0.522$ m respectively. A comparable improvement in fit to nadir altimetry and in situ WSE is also obtained in "N4l.CalVal" configuration, with a simulation error on WSE within [-0.5, 0.5]m for 87% of the data points and within [-0.25, 0.25]m for 69% of the data points. The 5 - th and 95 - th errors percentiles are  $\epsilon_{Q5} = -0.9$ m and  $\epsilon_{Q95} = 0.46$ m respectively.

This represents a significant improvement of the fit to SWOT WSE used in calibration, that are 600 times denser in space and time than nadir altimetry and in situ data used in "N4l.CalVal" experiment (179,192 data points in space and time with SWOT compared to 5,467 for nadir altimetry and in situ WSE). The similar fit obtained in the two configurations highlights the strength of our approach for integrating heterogeneous data of different sparsity.

Interestingly, over the shorter time window studied here and this assimilation of SWOT data only in "SWOT.CalVal", or of nadir altimetry and in situ WSE in "N4l.CalVal", both result in an improvement of the discharge (not assimilated, challenging to estimate) simulated at gauging stations within the hydraulic domain  $\Omega_{hy}$  (cf. Figure 10). Both experiments lead to significant discharge improvements at internal gauges. The nrmse on discharge at those internal gauges ranges in [0.05; 0.18] for "SWOT.CalVal" and [0.06; 0.22] "N4l.CalVal" while prior discharge nrmse is in [0.17; 0.34]. This further validates our approach, using WSE data from different altimetry missions and in combination or not with in situ WSE.



This improvement in terms of internal discharge, but also of the fit to the WSE assimilated, represent a good result for this challenging inference in the declining limb of a strong flood not reproduced by the hydrological model (grey dashed hydrographs) hence providing unfavourable prior inflows for VDA (black dashed hydrographs simulated by  $\mathcal{M}(\boldsymbol{\theta}_{SWOT}^{(0)})$  with both under and over estimations of real discharge which is a challenging case for VDA).

Moreover, for each gauge, comparable discharge improvements are obtained between the two experiments, in part because they are started from similar discharge background (but different prior bathymetry). But above all this outlines that sufficient information is contained in both altimetry datasets to constrain the sought parameters of the hydraulic model over the river network.

The optimized parameter  $\hat{\boldsymbol{\theta}}_{SWOT}$ , including inflow discharge hydrographs, spatialized bathymetry and friction over the river network hydraulic domain, are summarized in Figure 9 for the "SWOT.CalVal" experiment. (Note: Controls for the "N4l.CalVal" experiment are detailed in the appendix G). Again, for most segments of the river network, substantial corrections of bathymetry and friction are obtained. Along with upstream inflow corrections, these adjustments enable an improvement fit of simulated flow to altimetry and in situ WSE data. Recall that inferring these parameters from WSE data- which pertains to all controls of a 1D Saint-Venant hydraulic model- involves dealing with local structural equifinality (due to parameters embedded into friction term  $S_f$  and having a correlated influence on simulated WS) and spatial equifinality, as analyzed in Garambois & Momnier (2015); Garambois et al. (2020); Larnier et al. (2020); Pujol et al. (2024). To address this ill-posed inverse problem, covariance matrices are used in the VDA algorithm (as for previous "N4l.2019" experiment) to achieve a regularizing effect. This effect includes preconditioning and spatial or temporal regularization, smoothing the estimated spatial or temporal quantities when they are denser than observations.

The inferred hydrographs and bathymetry-friction profiles for each segment of the network are shown in appendix G. Detailed spatial parameters variabilities can be inferred thanks to the spatial density of SWOT data, which will be analyzed and compared to the inference with the nadir altimetry WSE data.

### 4.3 Detailed analysis of inferred parameters

The inferences of spatio-temporal parameters for the river network hydraulic model were performed from 2 datasets with significantly different spatio-temporal density, with the SWOT dataset being much denser in space and time. The bathymetry-friction profiles inferred over the Maroni main stream, specifically for the river network segments  $s = (1, 3, 5, 9, 12, 16, 18, 22, 23)$  as shown in Fig.6, are compared in Figure 12. This comparison includes inferences made using water surface elevation (WSE) data from nadir altimetry and gauges, as well as from SWOT data alone.

Both assimilation experiments "N4l.2019" and "SWOT.CalVal", result in the inference of spatially distributed bathymetry-friction over the network, along with corrections to upstream inflows. It is important to recall that those estimations are performed from different priors, either  $\boldsymbol{\theta}_{N4l}^{(0)}$  or  $\boldsymbol{\theta}_{SWOT}^{(0)}$ , based on the median discharge used

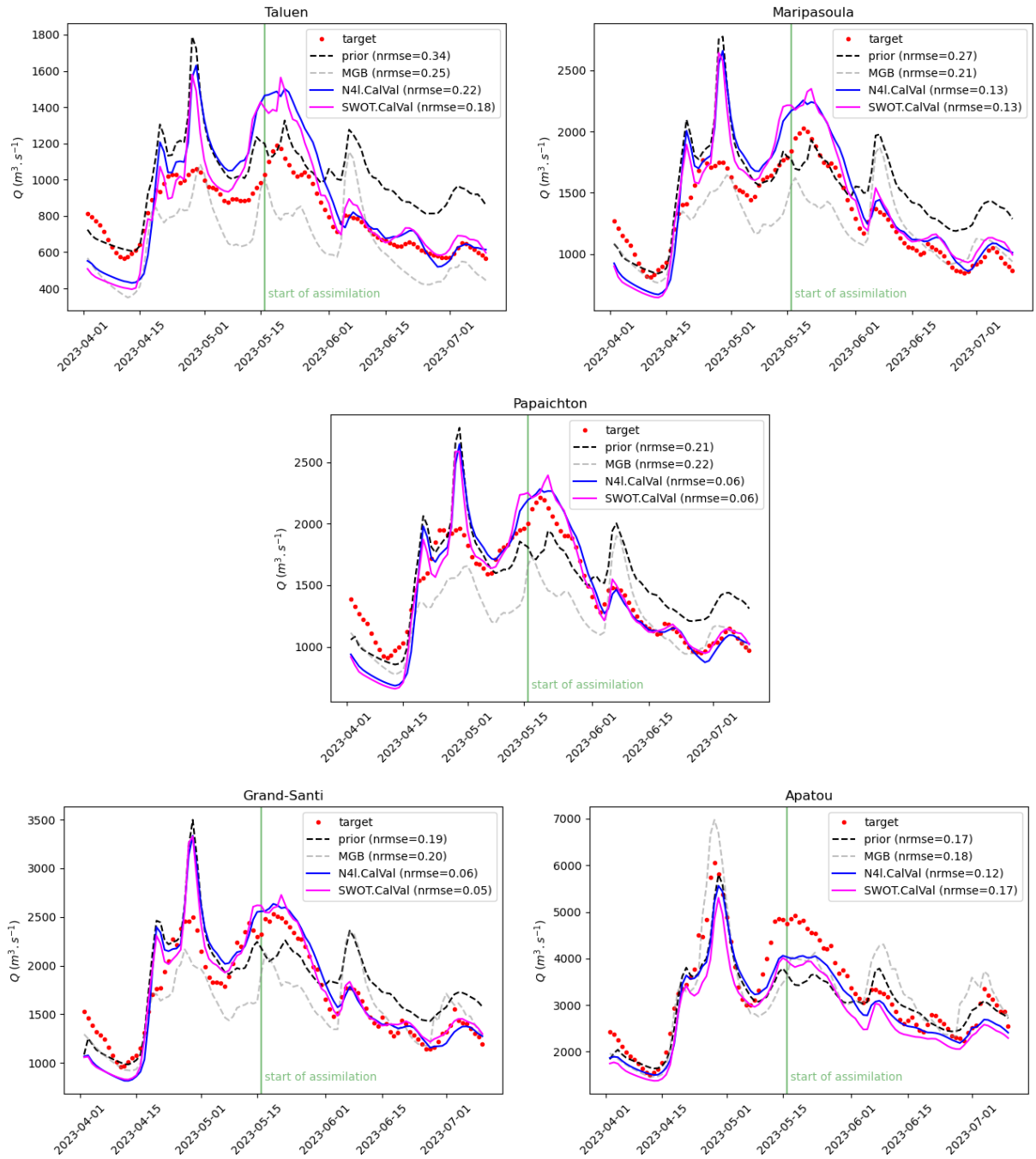


**Figure 10.** Validation of the calibrated Saint-Venant river network model on CalVal period in 2023: simulated discharge at internal gauges along the Maroni main stream following the assimilation over the Maroni Network of SWOT 1day altimetry or nadir altimetry and in situ WSE data in N4I configuration. The nRMSE ranges from 0.06 at the Grand-Santi and Papaïchton stations to 0.22 at the Taluen station for the N4I.CalVal experiment and from 0.05 at the Grand-Santi station to 0.18 at the Taluen station for the SWOT.CalVal experiment.

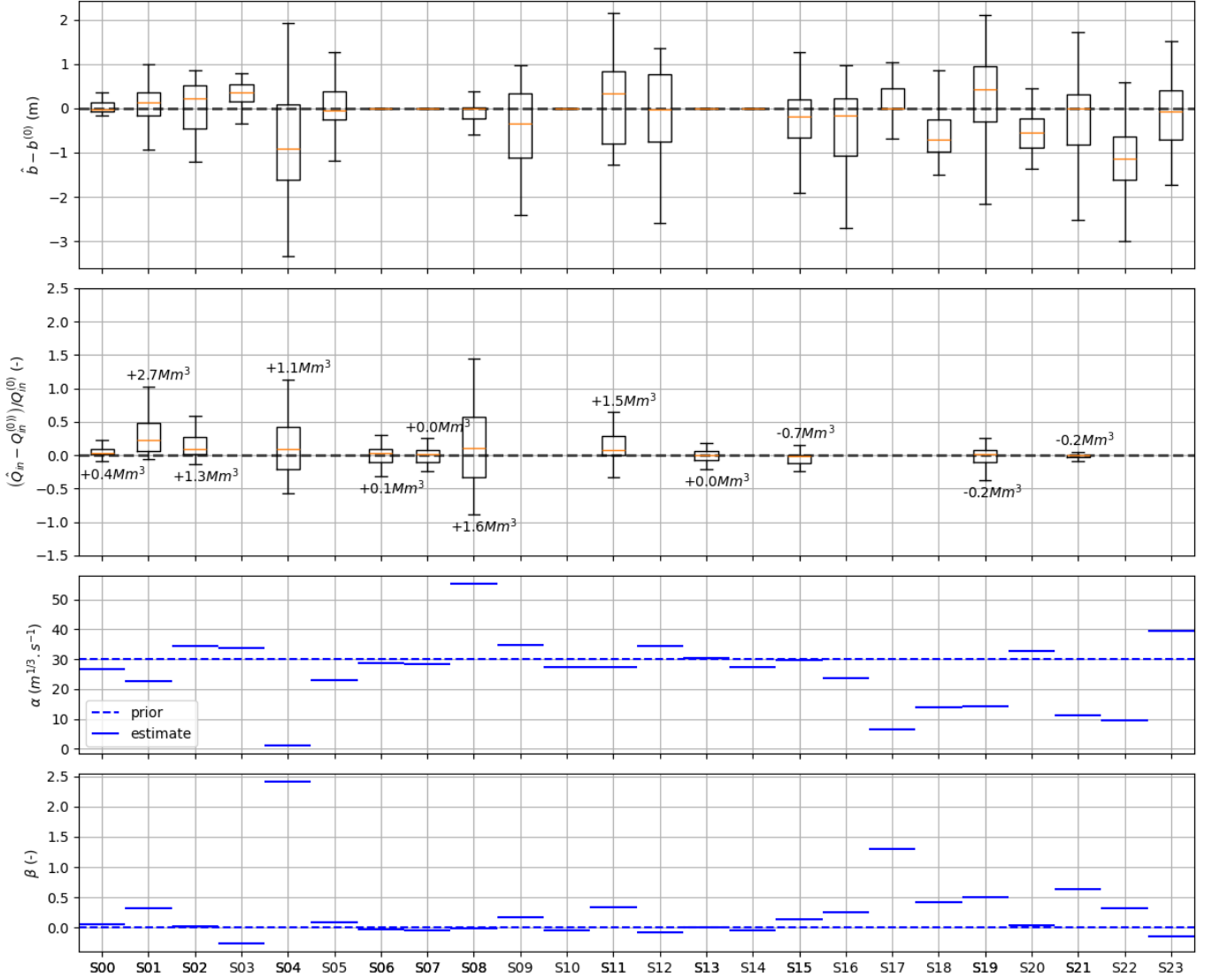


**Figure 11.** Relative correction of hydraulic model parameters after assimilation of SWOT WSE data in the experiment "SWOT.CalVal". The figure shows inferred parameters  $\hat{\theta}$  by VDA from the background  $\theta_{SWOT}^{(0)}$ , represented by segment of the river network "S00" to "S23": boxplots of spatially distributed corrections (top) of bathymetry  $b(s, x)$  at  $N_b = 2572$  hydraulic cross sections and of (second) inflow discharge hydrographs  $Q_{in, u=1..N_{BC}}^{t=1..T_u}$  at  $N_{BC} = 12$  inflows, (third and fourth) friction parameters  $\hat{\alpha}$  and  $\hat{\beta}$  over the 24 segments composing the simulated river network.

563 to infer prior bathymetry as explained before. Moreover, both experiments are performed with identical setup for  
564 covariance matrices, for weights  $\sigma_{\square}$  and correlation length  $L_{\square}$ .

565 The inferred parameters of the hydraulic model represent optimal solutions of the inverse problem (Equation  
566 9) given the WSE data considered. These parameters effectively describe the bathymetry, friction and inflows that  
567 achieve the best fit to the WSE data used.

568 The calibrated hydraulic models obtained can be utilized to derive stage-fall-discharge laws for operational  
569 discharge forecasting using SWOT WSE and WS slopes (cf. Malou et al. (2021)). Additionally, a network scale  
570 hydrological-hydraulic approach is relevant for upgrading SWOT discharge products, and will be used in future  
571 research on HiVDI Larnier et al. (2020). These upgrades would benefit from better constraints on the double re-  
572 gionalization problem, which involves estimating uncertain or unknown spatio-temporal hydrological and hydraulic  
573 parameters from sparse data.

574 All assimilation experiments, using the same channel width data  $W^*$ , result in the inference of non-trivial  
575 channel hydraulic controls (cf. definition in Montazem et al. (2019)). These controls are depicted in Figure 12 and  
576 in the flow profiles by segment in Appendix G). The inferred controls enable the production of more realistic WS  
577 signatures with respect to the assimilated WSE data, in the sense of the observation cost function. Notably, More  
578 spatial variations are obtained in the bathymetry inferred with the denser SWOT data.

579 Regarding inflow correction, this study only considered upstream inflows, which correspond to 36% of the  
580 basin drainage area. The inference of the remaining numerous lateral inflows, which vary in magnitude depending  
581 on their corresponding drainage area and forcing, is a challenging issue (cf. Pujol et al. (2020) for an analysis  
582 of frequential identifiability of inflows, see also Brisset et al. (2018)). This aspect should be addressed in further  
583 research.

584 The transposability of the hydraulic parameters obtained with the VDA approach would be feasible and  
585 coherent if they were calibrated simultaneously with hydrological model parameters. This simultaneous calibration  
586 could be used for temporal extrapolation. More generally, this pertains to the difficult issue of joint optimization  
587 of spatio-temporally distributed parameters of a H&H model.

588 Such an approach would be feasible with the present VDA method applied to a differentiable H&H solver as  
589 proposed in Pujol et al. (2022). Additionally, these approaches would benefit from differentiable regionalization  
590 schemes included into the forward model to map physical descriptors onto model parameters. This has been  
591 demonstrated with a regionalization neural network in Huynh et al. (2023) or even with a learnable spatially  
592 distributed hydrological model on top of a differentiable hydraulic model (Huynh et al., 2024). These elements are  
593 key components of a learnable, basin-scale physical model that can effectively integrate satellite hydraulic visibility.

## 594 5 Conclusion

595 This article presents a novel study on enhancing river network scale hydrological-hydraulic (H&H) models, by  
596 leveraging the unprecedented hydraulic visibility from the recently launched SWOT satellite. This is complemented

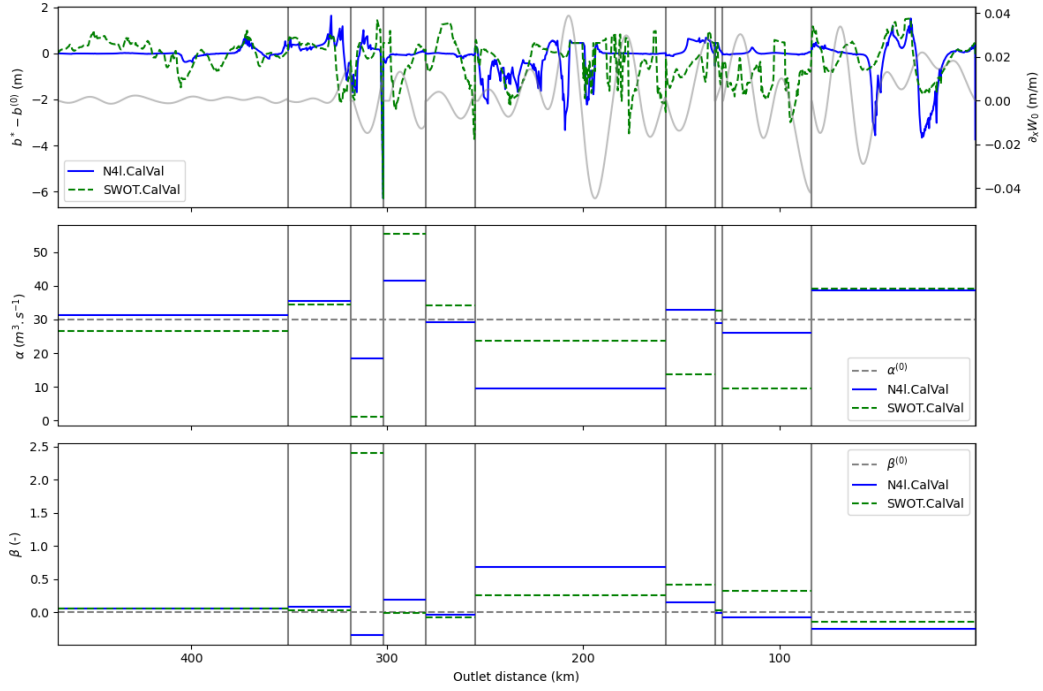


**Figure 12.** Longitudinal profiles along the Maroni main stream, segments  $s = (1, 3, 5, 9, 12, 16, 18, 22, 23)$ , of calibrated parameters after VDA: bathymetry  $\hat{b}$  and friction coefficients  $\alpha$  and  $\beta$ , along with channel width gradient  $\partial_x W_0$  (grey line), for the "N4I.CalVal" experiment (blue) and "SWOT.CalVal" experiment (dashed green).

597 by altimetry and imagery from other state-of-the-art satellites used to build the prior model geometry. A processing  
 598 chain is proposed for the construction of a consistent prior hydraulic model geometry using multi-satellite data,  
 599 including accurate images for dynamic water extents and a hydrological model. This work presents, for the first time  
 600 to our best knowledge, a VDA process over a river network hydraulic model fed by a semi-distributed hydrological  
 601 model, in a poorly gauged basin. Based on the obtained results and from the performed analysis, the following  
 602 conclusions can be drawn:

- 603 • The proposed variational approach represents a powerful optimization and diagnostic tool for differentiable  
 604 H&H models and spatio-temporal parameters estimation problems using multi-source data. The gradient  
 605 values  $\nabla_{\theta} j(\theta)$ , enable to analyze spatially distributed sensitivity maps of simulated quantities (with respect  
 606 to some parameters present in the parameter vector  $\theta$ ). Moreover, such gradient maps can be used to esti-  
 607 mate Sobol total sensitivity indices following the derivative-based sensitivity measure (DGSM) methodology  
 608 introduced in Sobol' & Kucherenko (2009), and applied using numerical adjoint models e.g. in lumped  
 609 hydrology in Chelil et al. (2022) or in 2D hydraulic modeling in Pujol et al. (2024).
- 610 • This study addresses the challenge of closing the ill-posed inverse problem of inferring river discharge from  
 611 water surface (WS) measurements alone, see Larnier et al. (2020). The method builds upon the HiVDI algo-  
 612 rithm (Larnier et al., 2020; Larnier & Monnier, 2023) focusing on single river portions, but achieves closure  
 613 of the ill-posed problem through the physical enrichment provided by sequentially coupling a hydrological

model with the hydraulic model over a complete river network. This approach uses the same computational tools and ingredients but leverages richer physical information and datasets at basin scale, enabling the closure of the problem.

This approach is applicable to other basins worldwide, utilizing open-source remote sensing data, for instance. This work opens up avenues for further research. Immediate to mid-term work perspectives include the following:

- Assimilation of SWOT science orbit data, which is sparser in time but provides nearly full spatial coverage at basin scale, both alone and in combination with other data available. This approach aims to investigate their informative power and address frequential inferability issues in detail, also considering large number of lateral inflows in function of available data.
- Application of the approach to gauged basins, utilizing massive datasets that include in situ measurements, drone data, and satellite observations.
- Studying how to improve SWOT discharge product using integrated basin scale H&H network models.
- Advanced data-model error accounting within Bayesian framework.
- Fully differentiable hydrological-hydraulic models (Pujol et al., 2022), incorporating learnable parts (Huynh et al., 2023), to enable simultaneous optimization of hydrological and hydraulic parameters from SWOT and other data. Such approaches would enable tackling the double H&H regionalization problem, where data are typically sparser than model parameters and rarely fully informative or constraining. For instance, even a lumped conceptual hydrological model faces equifinality issues when calibrated from a discharge time series.

The computational software used in this work is open source [DassFlow \(2023\)](#) The computation kernel written in Fortran is wrapped in Python. This enables the use of diverse libraries for signal processing, geographical treatments and machine learning, facilitating the development of hybrid deterministic-ML methods in its VDA framework (which enable large-dimensional parameter identification or calibration).

## 6 Appendix

### A H&H model and numerical resolution

A semi-distributed hydrological model  $\mathcal{M}_{rr}$  provides spatio-temporal discharges estimates  $Q_{rr}(x', t)$ ,  $\forall x' \in \Omega_{rr}, \forall t \in [0, T]$ . These estimates are used to inflow the hydraulic model at  $N_{in}$  inflow points, including upstream boundary conditions and lateral inflows, at the border of the hydraulic domain  $\Omega_{hy}$ .

The Saint-Venant equations are solved on each segment of the river network, and the continuity of the flow between segments is ensured by applying an equality constraint on water levels and mass conservation at the confluence between two segments.

Boundary conditions (BCs) are classically imposed (subcritical flows here) at boundary nodes (main hydrological inflows here) with inflow discharges  $Q_{in, i=1..N_{BC}}(t)$  at  $N_{BC}$  upstream nodes and WSE  $Z_{avl}(t)$  at the downstream node; lateral hydrographs  $q_{lat, i=1..N_{lat}}(t)$  at  $N_{lat}$  lateral inflow nodes (such that  $N_{in} = N_{BC} + N_{lat}$ ). The initial condition is set as the steady state backwater curve profile  $Z_0(x) = Z(Q_{in}(t_0), q_{lat, 1..L}(t_0))$  for hot-start. This

648 1D Saint-Venant model is discretized using the classical implicit Preissmann scheme (see e.g. [Cunge et al. \(1980\)](#);  
649 [Roux \(2004\)](#)) on a regular grid of spacing  $\Delta x$  using a double sweep method enabling to deal with flow regimes  
650 changes. An hourly time step  $\Delta t$  is used. This model is implemented into the computational software [DassFlow1D](#).  
651 [For more details](#) see DassFlow documentation (<https://dasshydro.github.io/doc/>); accurate finite volume scheme  
652 are also available; source code on GitHub (<https://github.com/DassHydro/dassflow1d>).

## 653 B Observation dataset

654 We denote by  $\mathbf{Y}^*$  the set of multi-source observations of hydraulic responses over the river network domain  
655  $\Omega_{hy}$ , which we aim to integrate into the flow model. This set includes in altimetric WSE and flow top width, which  
656 are unevenly spaced but cover the entire spatial domain densely. These observations come from various sources  
657 such as imagery, drifting or wide swath altimetry, in addition to multi-mission nadir altimetry.

658 In the general case, a multi-satellite dataset, composed of WS elevation and width observations, can be written  
659 as:

$$\mathbf{Y}^* := \left\{ (Z^*((s, x)_{vs=1..N_z}, t_{pz=1..P_z(oz)}); W^*((s, x)_{ws=1..N_w}, t_{pw=1..P_w(ow)})) \right\} \quad (\text{B1})$$

660 with  $(s, x)_\square$  denoting the spatial location of WSE or WSW measurements sorted in ascending, and  $t_\square$  representing  
661 the observation times at these location.  $N_z$  and  $N_w$  represent the number of WSE and WSW observation points  
662 accross the river network domain  $\Omega_{hy}$ , respectively.  $N_{oz}$  and  $N_{ow}$  represent the number of observation times  
663 for each WSE measurement location  $x_{oz=1..N_z}$  and WSW location  $x_{ow=1..N_w}$  respectively. Similarly,  $t_\square$  denotes  
664 measurements times.

665 In the case of SWOT,  $Z$  and  $W$  measurements are synchronous in time and space, and the dataset simplifies  
666 to:

$$\mathbf{Y}^* := (Z^*, W^*)(x_{o=1..N_o}, t_{p=1..p(o)}) \quad (\text{B2})$$

667 In this work, SWOT data are not used for geometry parameterization but only in assimilation. WS width are  
668 determined from dynamic water masks are extracted from Sentinel radar data. This enables the definition of XSs  
669 geometries.

## 670 C Regularization for the Variational data assimilation algorithm

671 The VDA algorithm is those developed in the HiVDI algorithm, see [Larnier et al. \(2020\)](#); [Larnier & Monnier](#)  
672 [\(2023\)](#); [DassFlow \(2023\)](#). The VDA formulation is based on covariance operators and the following change of  
673 control variable (see e.g. [Haben et al. \(2011\)](#); [Larnier et al. \(2020\)](#)):  $k = B^{-1/2} (\boldsymbol{\theta} - \boldsymbol{\theta}^{(0)})$ .  
674

675 The background  $\boldsymbol{\theta}^{(0)}$  (first guess, or prior in statistics) on the sought parameter from which optimization is  
676 started, and the background error covariance matrix  $B$ , both depend on the information available and a priori  
677 physical knowledge of the system and of the unknowns. With this change of control variable we are interested in

678 the minimization of the following cost function:  $j(\mathbf{k}) = \frac{1}{2} \left\| \mathcal{M}(\boldsymbol{\theta}^{(0)} + B^{1/2}\mathbf{k}) - Y^* \right\|_O^2$ .

679 The choice of  $B$  is crucial for the optimization and influences the inferred solution.

680 Assuming uncorrelated unknowns, the matrix  $B$  is block diagonal:  $B = \text{diag}(B_Q, B_b, B_K)$ . each block  $B_{\square}$   
681 being defined from the decreasing exponential kernels following [Malou & Monnier \(2022\)](#):

$$(B_Q)_{i,j} = (\sigma_Q)^2 \exp\left(-\frac{|t_j - t_i|}{L_Q}\right); \text{ and } (B_b)_{i,j} = (\sigma_b)^2 \exp\left(-\frac{|x_j - x_i|}{L_b}\right); \text{ and } B_K = \text{diag}(\sigma_\alpha^2, \sigma_\beta^2) \quad (\text{C1})$$

682 with  $L_Q$  and  $L_b$  acting as correlation scales defined a priori from empirical physical knowledge. The scalar values  
683  $\sigma_{\square}$  define the weighting effect in parameters optimization.

## 684 **D Processing algorithm for ICESat-2 ATL13 data to extract WSE**

685 ATL13 data is positionned along 6 beams (organized by pairs gt1r/gt1l, gt2r/gt2l, gt3r/gt3l) and presented  
686 as a set of beam-points (referenced by their longitude and latitude) above inland water bodies such as rivers and  
687 lakes only. Our goal is to aggregate this data to build WSE timeseries at virtual station over the Maroni river.  
688 For this purpose, we need a set a line geometry representing the river network centerline and a polygon geometry  
689 delineating the a priori watermask where ATL13 data will be extracted and processed.

### 690 **D1 Delineating the study domain watermask**

691 The watermask is taken from the Pekel's global Surface Water Dataset, considering water pixels with an  
692 occurence of at least 50%. This is an adequate hypothesis given the relatively low variability of top width found  
693 on the Maroni. This was confirmed by analyzing Sentinel 1-derived WSW of dynamic water masks obtained with  
694 ExtractEO chain.

695 For the studied Maroni basin, we considered and applied the following steps:

- 696 1. Polygonize Pekel watermask,
- 697 2. Application of a buffer with distance 0.0003 degree (as Pekel mask resolution is of 0.00025 degree): buffer  
698 function extends the boundaries of a given geometry and rounds its egde by the input distance.
- 699 3. Manual correction to fill missing river branches based on expert knowledge. Also, it was chosen to fully  
700 include under the watermask braided zone without distinguishing the individual river branches.
- 701 4. Cascaded union to merge individual polygons that intersect together
- 702 5. Small tributaries not represented by the Pekel product are added by building a polygon from a buffer around  
703 the riverline of those small tributaries and merging them to the rest of the domain (for the Maroni domain  
704 only).

### 705 **D2 WSE data extraction**

706 ICESat-2 products are organized by granule containing data below a full orbit, each orbit being divided in  
707 6 beams (gt1l/gt1r/gt2l/gt2r/gt3l/gt3r). A individual ICESat-2 is a beam point characterized by its coordinates



(lon, lat) and an elevation wse (above the WGS84 ellipsoid). ICESat-2 have to be extracted and aggregated under virtual stations to derive elevation timeseries and Xs for the effective hydraulic model.

For each granule, the following processing is applied:

1. Extraction of all beam points within the study domain polygon
2. Each beam point is "projected" along the river centerline. From this linear referencing, a curvilinear abscissa  $x_s$  [m] (distance along the centerline from the upstream edge) and a distance-to-the-river  $d_r$  [m] (distance between the original beam point and its projection) are associated to each beam point.
3. Then, each beam point is associated to the closest virtual station according to their  $x_s$ . A distance  $d_s$  ( $=x_{s,VS} - x_s$ ) and an angle ( $=\arctan \frac{d_r}{d_s}$ ) are derived accordingly.
4. Once all beam points are extracted, potential outliers have to be detected and flagged out for further processing (see appendix D3)
5. For each virtual station, time-aggregation is easily done by gathering beam points that comes from the same granule and the same cycle.
6. subsequently, beam points gathered in the same time index are spatially-aggregated into a single elevation measurements (see appendix D3)

### D3 More details on the processing of ATL13 data

#### D31 Outlier detection

Each river segment is divided into sub-segments of 5 km. Over each sub-segment, monthly subset of beam points which  $x_s$  fall on this sub-segment, are inspected. A linear regression of the elevation with respect to  $x_s$  from the ICESat-2 beam points subset is estimated with the standard deviation  $\sigma$  of the gap between the measured elevation and the corresponding (with respect to  $x_s$ ) elevation from the linear regression. All points that are above  $3\sigma$  are flagged out as outliers.

#### D32 Space aggregation

##### D322 Version 1

Every beam point attributes (ie. wse, lon, lat,  $x_s$ ,  $d_s$ ,  $d_r$ , angle, dt as seconds from Jan 1st, 2028) are simply averaged with a classical mean

##### D322 Version 2

Weighted averaged where each beam point weight  $w$  is defined by

$$w = 1. - \left\| \frac{d_s}{d_{s,max}} \right\|$$

## D322 Draw XSs

For each segment and its associated subdomain polygon

1. the domain polygon is split into voronoi regions centered around the virtual stations of the polygon. Each region delineates any beam point which the closest virtual station is the region's associated virtual station.
2. The XSs is draw following the constraint below:
  - The section is contained within the associated voronoi region
  - The section contains the virtual station
  - The section should cross the river with an angle close to normal to the river centerline
  - The section have to cross any region boundaries that are common with the overall polygon exterior boundaries

If one can not draw a XS that respects the constraints above, a section normal to the river centerline is drawn with a width equal to the largest  $d_r$ .

## E Processing of watermarks images to extract river width

River widths were extracted from a collection of 121 watermarks computed using the ExtractEO algorithm (Maxant et al. (2022)) on available Sentinel 1 images for the period 2021-01-01 - 2022-12-31. The river widths were computed using the dedicated BAS algorithm (<https://github.com/CS-SI/BAS>). The methodology is fully applicable on other zone of interest, even with watermark computed from other water classification algorithm (provided as binary classification where water is 1 and land,etc. is 0).

These widths are usable for non rectangular XS parameterization but a simple rectangular XS is sufficient for this study on the Maroni River. More complex XSs have been used on the Niger basin, leading to a model setup that enables good realism. However, this is not presented here and left for further research. Note that the vertical referencing of these dynamic water extents over time can be performed with altimetric measurements around image acquisition date while simultaneous WSE and WSW measurement are obtained with SWOT.

## F SWOT L2 wavelet based filtering and segmentation algorithm

The wavelet-based filtering and segmentation algorithm is designed to process WSE longitudinal profiles, such as those provided by SWOT or by in situ GNSS, while preserving the WS signatures of hydraulic controls (HCs). This algorithm is based on the approach and MATLAB codes of Montazem et al. (2019). The idea is to use wavelet processing to isolate the signatures of local hydraulic controls (HCs), as hydraulic variability manifests at multiple spatial scales. Using a wavelet basis allows for the decomposition of free surface spatial profiles with high accuracy while retaining localized frequency information. A unique feature of this approach is the use of wavelets to both denoising and segmenting (not used here) signals in a consistent, space-frequency localized manner. This method introduces minimal oscillations into the reconstructed filtered signal and is well suited for unsteady signals and detecting strong curvature signals. This algorithm, called pyrscwt (Python River Segmentation with Continuous

769 Wavelet Transform), is based on a custom Python implementation of a continuous wavelet transform, enabling  
770 accurate 1D signal projections and reconstructions.

771 The proposed algorithm aims to (i) efficiently denoise L2 SWOT-type river node-scale data (RiverObs product  
772 at spatial resolution  $dx \sim 200m$ ), (ii) perform a segmentation of a river portion into reaches, at user defined scale,  
773 that best preserves hydraulic signals and ultimately contributes to the quality of flow modeling and its coherence  
774 with multi-mission altimetry data. In the present article only denoising of SWOT RiverObs WSE  $Z(x)$  data is  
775 performed with pyrschw before their assimilation into the hydraulic model at local XS scale.

776 The proposed algorithm taking as input a spatial signal of WSE  $Z(x)$  signals, sampled at a constant spatial  
777 step, consists in the following steps:

- 778 • Signal resampling and symmetrization (prolongation of the signal on its spatial borders).
- 779 • Automated choice of the wavelet projection basis (7 mother wavelets and 10 orders for each) such that the  
780 reconstruction error  $\epsilon_{\hat{Z}}$  is minimal.
- 781 • Filtering and segmentation of the original signal  $Z(x)$  obtained by a low-pass filtering of wavelet coefficients  
782 corresponding to spatial variations below a user defined cutoff length scale  $\lambda_c$ . An additional physical criterion  
783 is used to filter wavelet coefficients: at the scale of measurements a counter slope in the WS is unphysical,  
784 that is  $\partial_x Z > 0$ . For a zone of length  $l_d$  with a counter slope we consider a centered window of length  $3l_d$ ,  
785 since we do not know whether this unphysical counterslope stems from over-underestimations upstream or  
786 downstream, on which wavelet coefficients are iteratively filtered until  $\partial_x \hat{Z} \leq 0$
- 787 • Hydraulic control sections (HCs) detection with the reconstructed signal  $\hat{Z}(x)$  that is "error free" via maxi-  
788 mum of WS curvature  $\partial_x^2 \hat{Z}(x)$ .

## 789 G Detail on inferred parameters

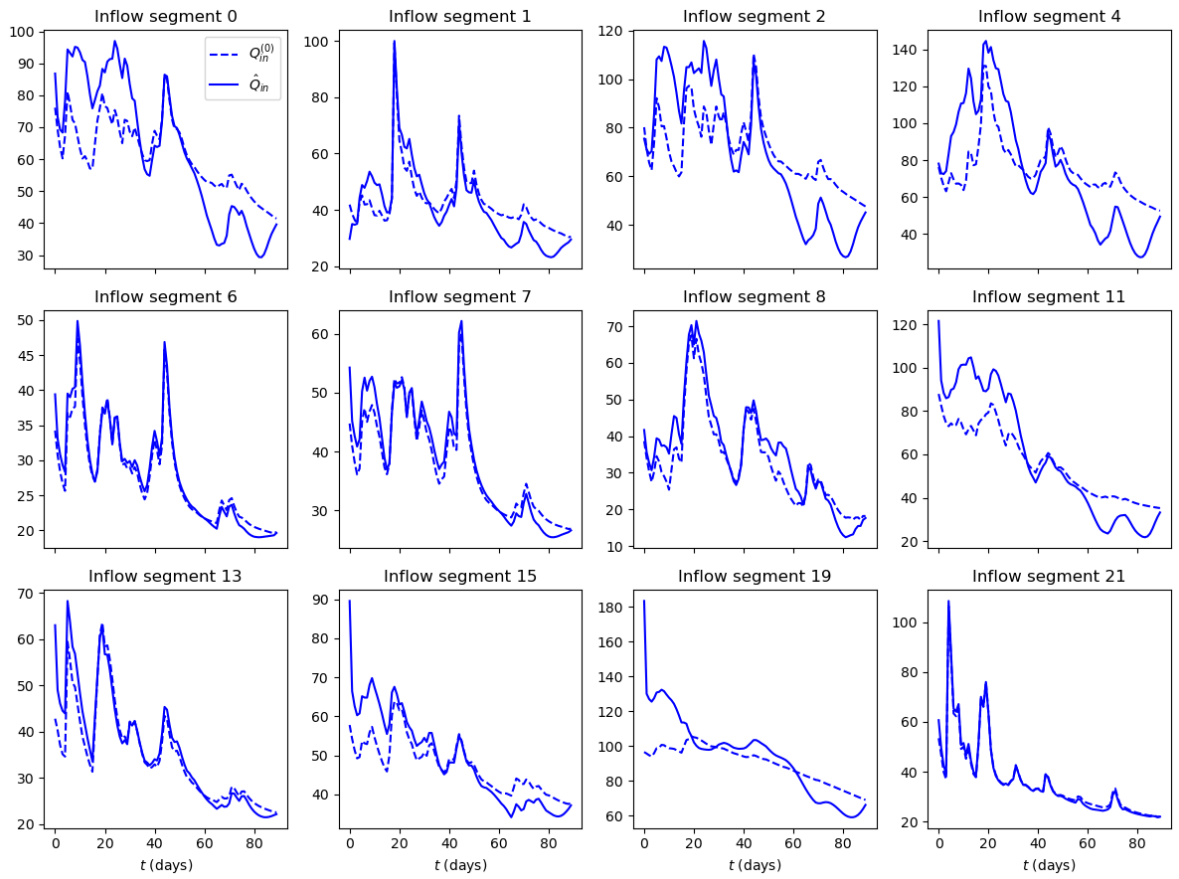


Figure G1. Inferred inflow hydrographs N41.2019

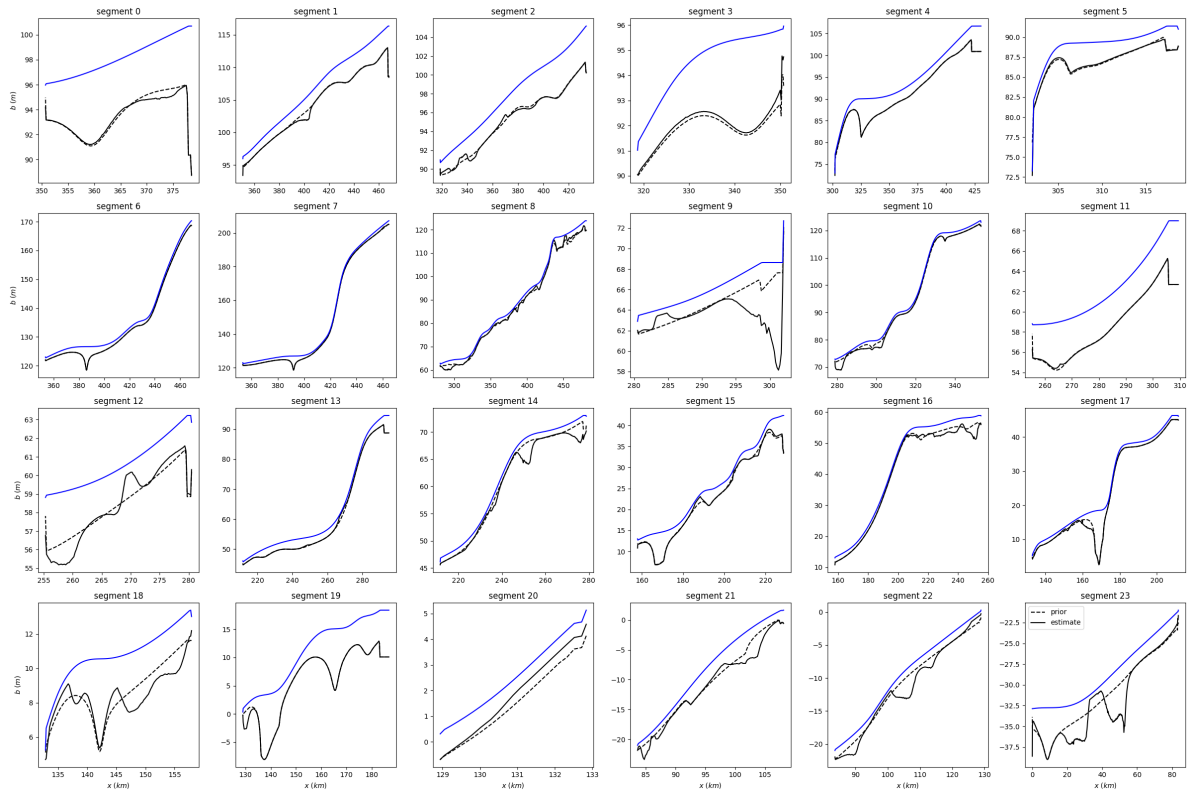
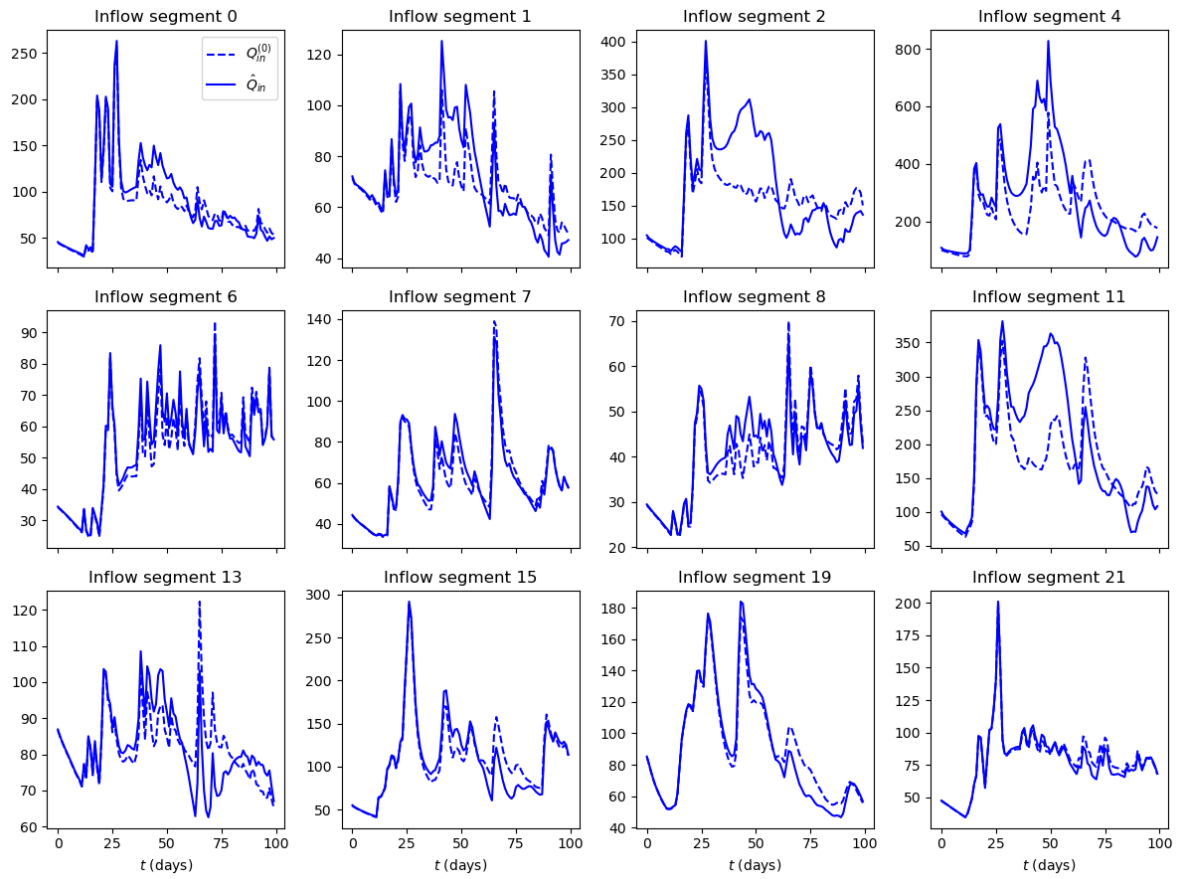
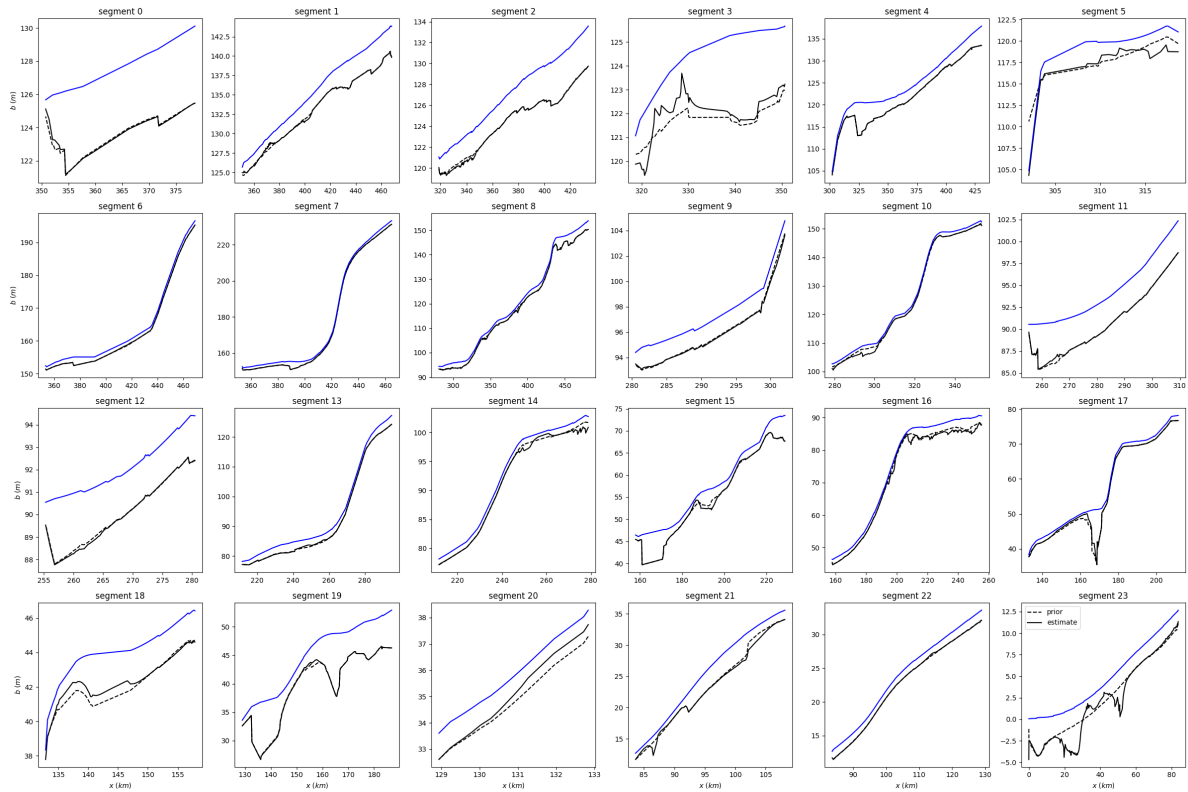


Figure G2. Inferred bathymetry N41.2019



**Figure G3.** Inferred inflow hydrographs N4I.CalVal



**Figure G4.** Inferred bathymetry N4I.CalVal

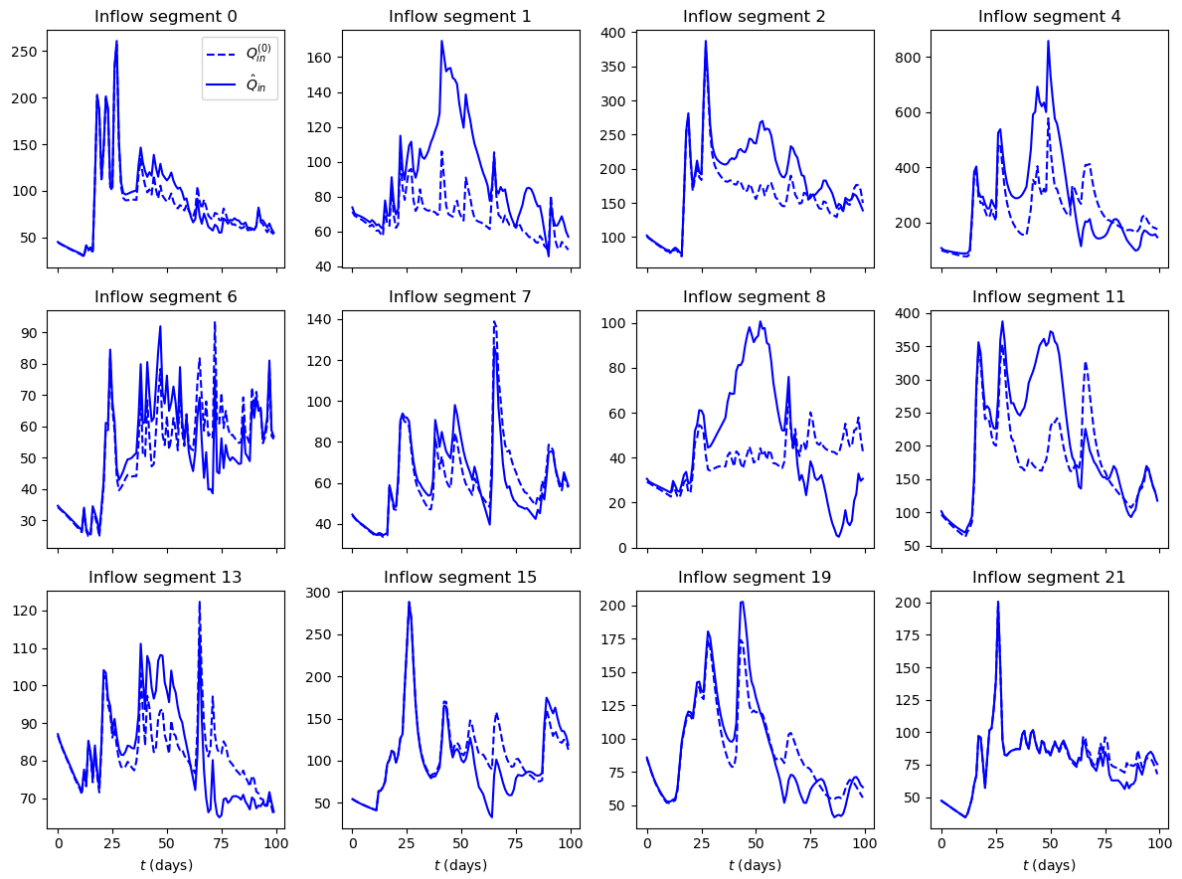


Figure G5. Inferred inflow hydrographs SWOT.CalVal

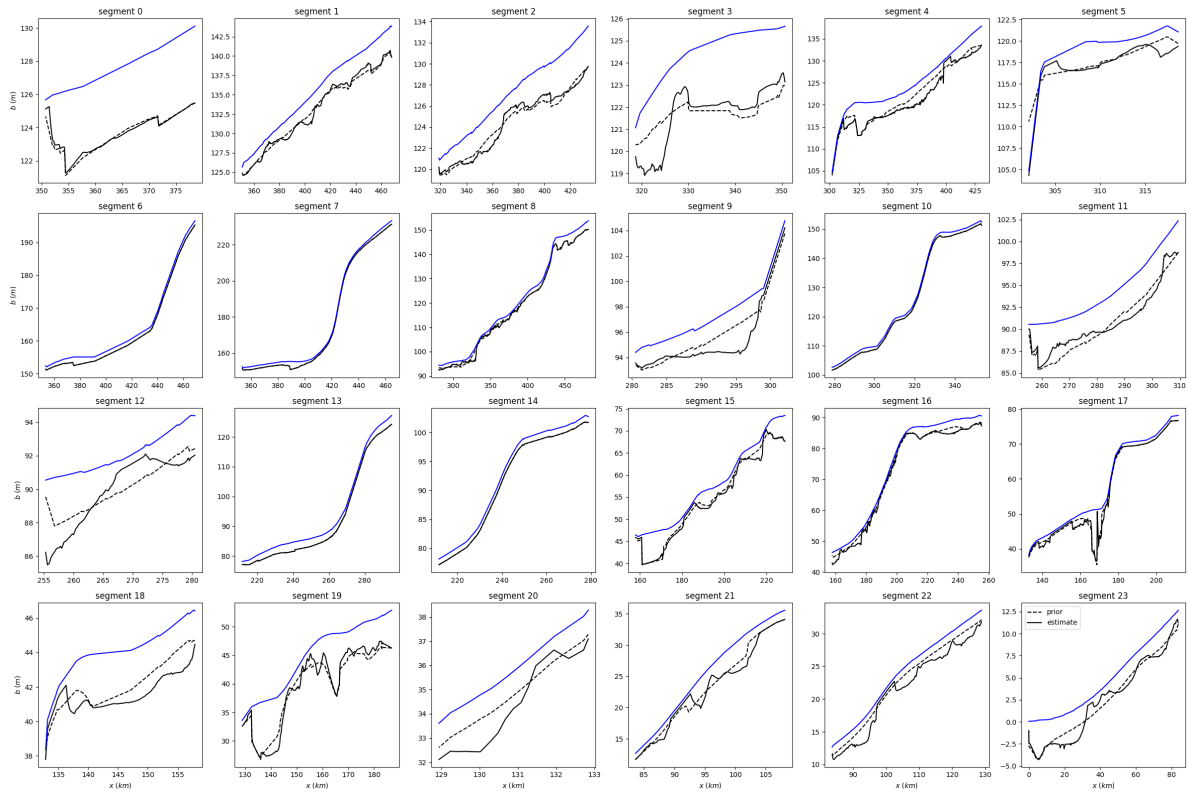


Figure G6. Inferred bathymetry SWOT.CalVal

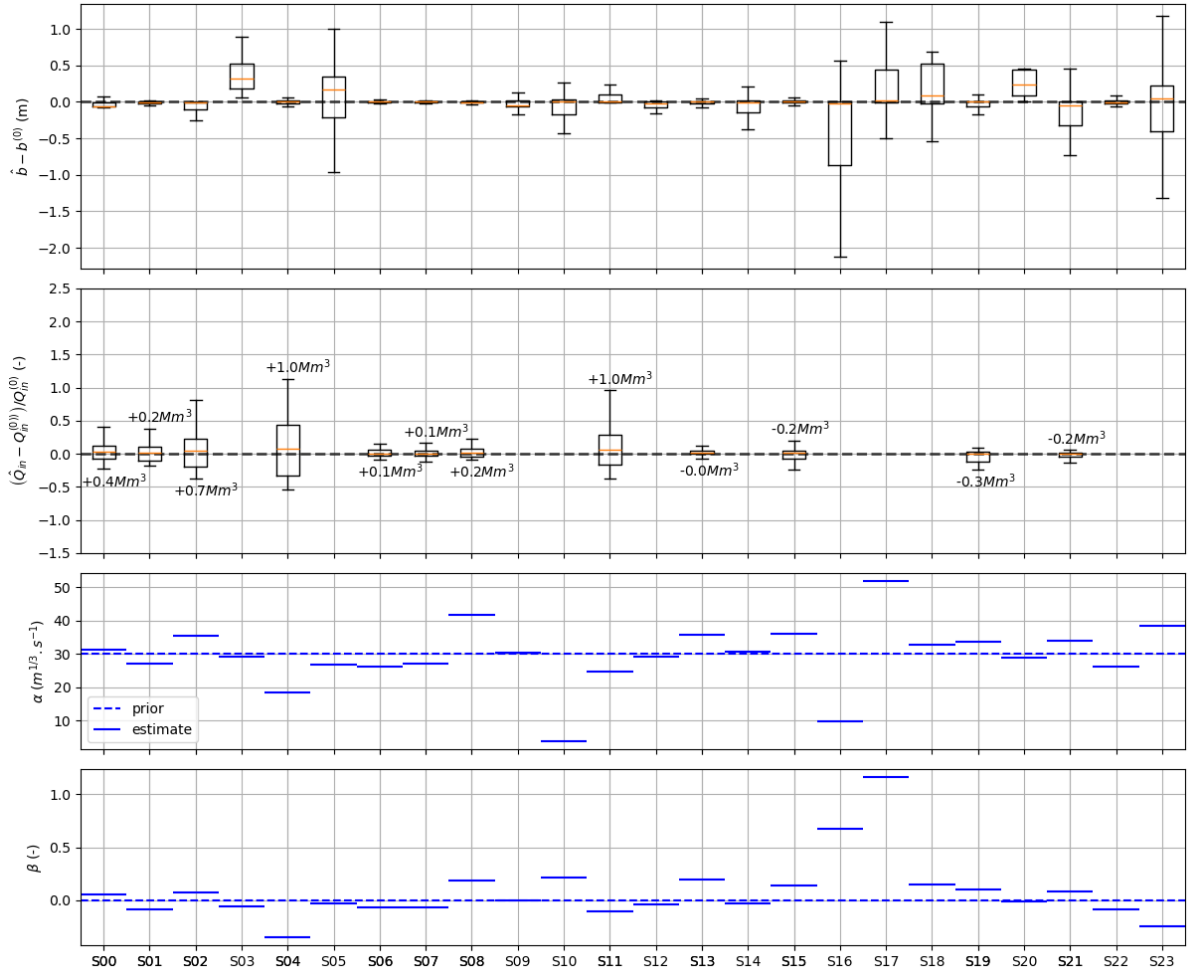


Figure G7. Model parameters  $\hat{\theta}$  inferred by VDA in the N41.CalVal experiment

## Open Research

*Data Availability Statement.* This article is based on open source data, dataset shareable upon request. *Software Availability Statement.* DassFlow source code is open source and available at <https://github.com/DassHydro/dassflow1d>. MGB is also an open source code.

## Acknowledgments

CNES for financial support of several authors, and also for engineering support regarding processing of WSW data and SWOT data. DEAL Guyane for processing discharge data. Evanne Angenent for data processing and contribution to the first modeling of the Maroni basin with MGB-DassFlow1D, during an internship at INRAE and DEAL Cayenne. Joao Hemptinne for participation to re-implementation of the segmentation algorithm.

*Authors contributions:* Design of this research: PAG, KL. Manuscript writing, conceptualization, analyses: PAG, KL and JM. Numerical results: KL. Preprocessing algorithms implementation: CE, KL. Data and/or hydrological modeling and/or review and editing of the manuscript: All.

## References

- Altenau, E. H., Pavelsky, T. M., Durand, M. T., Yang, X., Frasson, R. P. d. M., & Bendezu, L. (2021). The surface water and ocean topography (swot) mission river database (sword): A global river network for satellite data products. *Water Resources Research*, *57*(7), e2021WR030054. Retrieved from <https://agupubs.onlinelibrary.wiley.com/doi/abs/10.1029/2021WR030054> (e2021WR030054 2021WR030054) doi: <https://doi.org/10.1029/2021WR030054>
- Andreadis, K. M., Brinkerhoff, C. B., & Gleason, C. J. (2020). Constraining the assimilation of swot observations with hydraulic geometry relations. *Water Resources Research*, *56*(5), e2019WR026611. Retrieved from <https://agupubs.onlinelibrary.wiley.com/doi/abs/10.1029/2019WR026611> (e2019WR026611 10.1029/2019WR026611) doi: <https://doi.org/10.1029/2019WR026611>
- Asch, M., Bocquet, M., & Nodet, M. (2016). *Data assimilation: methods, algorithms, and applications* (Vol. 11). SIAM.
- Bonnans, J. F., Gilbert, J. C., Lemaréchal, C., & Sagastizábal, C. A. (2006). *Numerical optimization: Theoretical and practical aspects*. Springer. Retrieved from <https://www.springer.com/gp/book/9783540354453>
- Brisset, P., Monnier, J., Garambois, P.-A., & Roux, H. (2018). On the assimilation of altimetric data in 1D Saint-Venant river flow models. *Advances in water resources*, *119*, 41-59. Retrieved from <https://doi.org/10.1016/j.advwatres.2018.06.004>
- Chelil, S., Oubanas, H., Henine, H., Gejadze, I., Malaterre, P. O., & Tournebize, J. (2022). Variational data assimilation to improve subsurface drainage model parameters. *Journal of Hydrology*, 128006.
- Chow, V. (1959). *Open-channel hydraulics*. New-York, USA: Mc Graw-Hill.
- Collischon, W., Allasia, D., Da Silva, B., & M., T. C. E. (2007). The mgb-iph model for large-scale rainfall—runoff modelling. *Hydrological Sciences Journal*, *52*(5), 878–895. Retrieved from <https://doi.org/10.1623/hysj.52>



- 824 .5.878 doi: 10.1623/hysj.52.5.878
- 825 Coppo Frias, M., Liu, S., Mo, X., Nielsen, K., Randall, H., Jiang, L., ... Bauer-Gottwein, P. (2022). River hydraulic  
826 modelling with icesat-2 land and water surface elevation. *EGUsphere*, 2022, 1–27. Retrieved from [https://  
827 egusphere.copernicus.org/preprints/2022/egusphere-2022-377/](https://egusphere.copernicus.org/preprints/2022/egusphere-2022-377/) doi: 10.5194/egusphere-2022-377
- 828 Cunge, J. A., Holly, M., F., & Verwey, A. (1980). *Practical aspects of computational river hydraulics*. Pitam  
829 Publishing,.
- 830 DassFlow. (2023). Data assimilation for free surface flows. open source computational code. Retrieved from  
831 <https://github.com/DassHydro>
- 832 Dingman, S. (2009). *Fluvial hydraulics*. Oxford University Press.
- 833 Dingman, S. L. (2007). Analytical derivation of at-a-station hydraulic–geometry relations. *Journal of Hydrology*,  
834 334(1), 17-27. Retrieved from <https://www.sciencedirect.com/science/article/pii/S0022169406005063>  
835 doi: <https://doi.org/10.1016/j.jhydrol.2006.09.021>
- 836 Dingman, S. L., & Afshari, S. (2018). Field verification of analytical at-a-station hydraulic-geometry relations.  
837 *Journal of Hydrology*, 564, 859-872. Retrieved from [https://www.sciencedirect.com/science/article/pii/  
838 S0022169418305250](https://www.sciencedirect.com/science/article/pii/S0022169418305250) doi: <https://doi.org/10.1016/j.jhydrol.2018.07.020>
- 839 Durand, M., Gleason, C. J., Pavelsky, T. M., Prata de Moraes Frasson, R., Turmon, M., David, C. H., ...  
840 Wang, J. (2023). A framework for estimating global river discharge from the surface water and ocean to-  
841 pography satellite mission. *Water Resources Research*, 59(4), e2021WR031614. Retrieved from [https://  
842 agupubs.onlinelibrary.wiley.com/doi/abs/10.1029/2021WR031614](https://agupubs.onlinelibrary.wiley.com/doi/abs/10.1029/2021WR031614) (e2021WR031614 2021WR031614) doi:  
843 <https://doi.org/10.1029/2021WR031614>
- 844 Durand, M., Neal, J., Rodríguez, E., Andreadis, K., Smith, L., & Yoon, Y. (2014). Estimating reach-averaged  
845 discharge for the river Severn from measurements of river water surface elevation and slope. *Journal of Hydrology*,  
846 511, 92-104. doi: 10.1016/j.jhydrol.2013.12.050
- 847 Eggleston, J., Mason, C., Bjerklie, D., Durand, M., Dudley, R., & Harlan, M. (2024). Siting considerations for satel-  
848 lite observation of river discharge. *Water Resources Research*, 60(6), e2023WR034583. Retrieved from [https://  
849 agupubs.onlinelibrary.wiley.com/doi/abs/10.1029/2023WR034583](https://agupubs.onlinelibrary.wiley.com/doi/abs/10.1029/2023WR034583) (e2023WR034583 2023WR034583) doi:  
850 <https://doi.org/10.1029/2023WR034583>
- 851 Flipo, N., Mouhri, A., Labarthe, B., Biancamaria, S., Rivière, A., & Weill, P. (2014). Continental hydrosystem  
852 modelling: the concept of nested stream&ndash;aquifer interfaces. *Hydrology and Earth System Sciences*, 18(8),  
853 3121–3149. Retrieved from <https://www.hydrol-earth-syst-sci.net/18/3121/2014/> doi: 10.5194/hess-18  
854 -3121-2014
- 855 Frasson, R. P. d. M., Durand, M. T., Larnier, K., Gleason, C., Andreadis, K. M., Hagemann, M., ... David, C. H.  
856 (2021). Exploring the factors controlling the error characteristics of the surface water and ocean topography  
857 mission discharge estimates. *Water Resources Research*, 57(6), e2020WR028519. Retrieved from [https://  
858 agupubs.onlinelibrary.wiley.com/doi/abs/10.1029/2020WR028519](https://agupubs.onlinelibrary.wiley.com/doi/abs/10.1029/2020WR028519) (e2020WR028519 2020WR028519) doi:  
859 <https://doi.org/10.1029/2020WR028519>

- 860 Garambois, P.-A., Calmant, S., Roux, H., Paris, A., Monnier, J., Finaud-Guyot, P., . . . Santos-da Silva, J. (2017).  
861 Hydraulic visibility: Using satellite altimetry to parameterize a hydraulic model of an ungauged reach of a  
862 braided river. *Hydrological Processes*, *31*(4), 756–767. Retrieved from <http://dx.doi.org/10.1002/hyp.11033>  
863 (hyp.11033) doi: 10.1002/hyp.11033
- 864 Garambois, P.-A., Larnier, K., Monnier, J., Finaud-Guyot, P., Verley, J., Montazem, A.-S., & Calmant, S.  
865 (2020). Variational estimation of effective channel and ungauged anabranching river discharge from multi-  
866 satellite water heights of different spatial sparsity. *Journal of Hydrology*, *581*, 124409. Retrieved from  
867 <https://www.sciencedirect.com/science/article/pii/S0022169419311448> doi: [https://doi.org/10.1016/](https://doi.org/10.1016/j.jhydrol.2019.124409)  
868 [j.jhydrol.2019.124409](https://doi.org/10.1016/j.jhydrol.2019.124409)
- 869 Garambois, P.-A., & Monnier, J. (2015). Inference of effective river properties from remotely sensed observations of  
870 water surface. *Advances in Water Resources*, *79*, 103-120. Retrieved from [https://www.sciencedirect.com/](https://www.sciencedirect.com/science/article/pii/S0309170815000330)  
871 [science/article/pii/S0309170815000330](https://www.sciencedirect.com/science/article/pii/S0309170815000330) doi: <https://doi.org/10.1016/j.advwatres.2015.02.007>
- 872 Gejadze, I., & Malaterre, P.-O. (2017). Discharge estimation under uncertainty using variational methods with  
873 application to the full saint-venant hydraulic network model. *International Journal for Numerical Methods in*  
874 *Fluids*, *83*(5), 405-430. Retrieved from <https://onlinelibrary.wiley.com/doi/abs/10.1002/fld.4273> doi:  
875 <https://doi.org/10.1002/fld.4273>
- 876 Gejadze, I., Malaterre, P.-O., Oubanas, H., & Shutyaev, V. (2022). A new robust discharge estimation method  
877 applied in the context of swot satellite data processing. *Journal of Hydrology*, *610*, 127909. Retrieved from  
878 <https://www.sciencedirect.com/science/article/pii/S002216942200484X> doi: [https://doi.org/10.1016/](https://doi.org/10.1016/j.jhydrol.2022.127909)  
879 [j.jhydrol.2022.127909](https://doi.org/10.1016/j.jhydrol.2022.127909)
- 880 Getirana, A. C. (2010). Integrating spatial altimetry data into the automatic calibration of hydrological models.  
881 *Journal of Hydrology*, *387*(3), 244-255. Retrieved from [https://www.sciencedirect.com/science/article/](https://www.sciencedirect.com/science/article/pii/S0022169410001988)  
882 [pii/S0022169410001988](https://www.sciencedirect.com/science/article/pii/S0022169410001988) doi: <https://doi.org/10.1016/j.jhydrol.2010.04.013>
- 883 Haben, S., Lawless, A., & Nichols, N. (2011). Conditioning of incremental variational data assimilation, with  
884 application to the met office system. *Tellus A*, *63*(4), 782-792.
- 885 Hascoet, L., & Pascual, V. (2013). The tapenade automatic differentiation tool: principles, model, and specification.  
886 *ACM Transactions on Mathematical Software (TOMS)*, *39*(3), 1–43.
- 887 Horner, I., Renard, B., Le Coz, J., Branger, F., McMillan, H. K., & Pierrefeu, G. (2018). Impact of Stage Measure-  
888 ment Errors on Streamflow Uncertainty. *Water Resour. Res.*, *54*(3), 1952–1976. doi: 10.1002/2017WR022039
- 889 Huynh, N. N. T., Garambois, P.-A., Colleoni, F., Renard, B., Roux, H., Demargne, J., & Javelle, P. (2023). *Learning*  
890 *regionalization within a differentiable high-resolution hydrological model using accurate spatial cost gradients*.
- 891 Huynh, N. N. T., Garambois, P.-A., Renard, B., Colleoni, F., Monnier, J., & Roux, H. (2024, February). Multiscale  
892 learnable physical modeling and data assimilation framework: Application to high-resolution regionalized hydro-  
893 logical simulation of flash floods. Retrieved from <http://dx.doi.org/10.22541/au.170709054.44271526/v1>  
894 doi: 10.22541/au.170709054.44271526/v1
- 895 Kubota, T., Aonashi, K., Ushio, T., Shige, S., Takayabu, Y. N., Kachi, M., . . . others (2020). Global satellite

- 896 mapping of precipitation (gsmap) products in the gpm era. *Satellite Precipitation Measurement: Volume 1*,  
897 355–373.
- 898 Lague, D., & Feldmann, B. (2020). Chapter 2 - topo-bathymetric airborne lidar for fluvial-geomorphology analysis.  
899 In P. Tarolli & S. M. Mudd (Eds.), *Remote sensing of geomorphology* (Vol. 23, p. 25-54). Elsevier. Retrieved  
900 from <https://www.sciencedirect.com/science/article/pii/B9780444641779000023> doi: <https://doi.org/10.1016/B978-0-444-64177-9.00002-3>
- 901
- 902 Larnier, K., & Monnier, J. (2023). Hybrid neural network - variational data assimilation algorithm to infer river  
903 discharges from swot-like data. *Comput. Geoscience*, 853–877. Retrieved from <https://doi.org/10.1007/s10596-023-10225-2>
- 904
- 905 Larnier, K., Monnier, J., Garambois, P.-A., & Verley, J. (2020). River discharge and bathymetry estimation from  
906 swot altimetry measurements. *Inverse Problems in Science and Engineering*, 1-31. Retrieved from <https://doi.org/10.1080/17415977.2020.1803858>
- 907
- 908 Le Coz, J., Renard, B., Bonnifait, L., Branger, F., & Le Boursicaud, R. (2014). Combining hydraulic knowledge and  
909 uncertain gaugings in the estimation of hydrometric rating curves: A bayesian approach. *Journal of Hydrology*,  
910 509, 573-587. Retrieved from <https://www.sciencedirect.com/science/article/pii/S0022169413008329>  
911 doi: <https://doi.org/10.1016/j.jhydrol.2013.11.016>
- 912 Leopold, L., & Maddock, T. (1953). The hydraulic geometry of stream channels and some physiographic implica-  
913 tions. *USGS Numbered Series*, 252, 57pp. Retrieved from <https://pubs.er.usgs.gov/publication/pp252>
- 914 Malou, T., Garambois, P.-A., Paris, A., Monnier, J., & Larnier, K. (2021). Generation and analysis of stage-fall-  
915 discharge laws from coupled hydrological-hydraulic river network model integrating sparse multi-satellite data.  
916 *Journal of Hydrology*, 603, 126993. Retrieved from <https://doi.org/10.1016/j.jhydrol.2021.126993>
- 917 Malou, T., & Monnier, J. (2022). Covariance kernels investigation from diffusive wave equations for data assimilation  
918 in hydrology. *Inverse Problems*. Retrieved from <https://doi.org/10.1088/1361-6420/ac509d> (Accepted)
- 919 Mansanarez, V., Le Coz, J., Renard, B., Lang, M., Pierrefeu, G., & Vauchel, P. (2016). Bayesian analysis of stage-  
920 fall-discharge rating curves and their uncertainties. *Water Resources Research*, 52(9), 7424-7443. Retrieved  
921 from <https://agupubs.onlinelibrary.wiley.com/doi/abs/10.1002/2016WR018916> doi: <https://doi.org/10.1002/2016WR018916>
- 922
- 923 Masson-Delmotte, V., Zhai, P., Pörtner, H.-O., Roberts, D., Skea, J., Shukla, P. R., et al. (2022). *Global warming*  
924 *of 1.5 c: Ipcc special report on impacts of global warming of 1.5 c above pre-industrial levels in context of*  
925 *strengthening response to climate change, sustainable development, and efforts to eradicate poverty*. Cambridge  
926 University Press.
- 927 Maxant, J., Braun, R., Caspard, M., & Clandillon, S. (2022). Extracteo, a pipeline for disaster extent mapping  
928 in the context of emergency management. *Remote Sensing*, 14(20). Retrieved from <https://www.mdpi.com/2072-4292/14/20/5253> doi: 10.3390/rs14205253
- 929
- 930 Meyer Oliveira, A., Fleischmann, A., & Paiva, R. (2021). On the contribution of remote sensing-based calibration to  
931 model hydrological and hydraulic processes in tropical regions. *Journal of Hydrology*, 597, 126184. Retrieved from

- 932 <https://www.sciencedirect.com/science/article/pii/S0022169421002316> doi: <https://doi.org/10.1016/>  
933 [j.jhydrol.2021.126184](https://doi.org/10.1016/j.jhydrol.2021.126184)
- 934 Milly, P. (1994). Climate, interseasonal storage of soil water, and the annual water balance. *Advances in*  
935 *Water Resources*, 17(1), 19-24. Retrieved from [https://www.sciencedirect.com/science/article/pii/](https://www.sciencedirect.com/science/article/pii/0309170894900205)  
936 [0309170894900205](https://www.sciencedirect.com/science/article/pii/0309170894900205) (MIT Colloquium on Hydroclimatology and Global Hydrology) doi: 10.1016/0309-1708(94)  
937 90020-5
- 938 Monnier, J. (2021). *Data assimilation, optimal control and learning*. Open Online Course, INSA Toulouse, France.
- 939 Montazem, A.-S., Garambois, P.-A., Calmant, S., Finaud-Guyot, P., Monnier, J., Medeiros Moreira, D., ...  
940 Biancamaria, S. (2019). Wavelet-based river segmentation using hydraulic control-preserving water sur-  
941 face elevation profile properties. *Geophysical Research Letters*, 46(12), 6534-6543. Retrieved from [https://](https://agupubs.onlinelibrary.wiley.com/doi/abs/10.1029/2019GL082986)  
942 [agupubs.onlinelibrary.wiley.com/doi/abs/10.1029/2019GL082986](https://agupubs.onlinelibrary.wiley.com/doi/abs/10.1029/2019GL082986) doi: 10.1029/2019GL082986
- 943 Nachtergaele, F., van Velthuisen, H., Verelst, L., Wiberg, D., Henry, M., Chiozza, F., ... others (2023). *Harmonized*  
944 *world soil database version 2.0*. FAO.
- 945 Oubanas, H., Gejadze, I., Malaterre, P.-O., & Mercier, F. (2018). River discharge estimation from synthetic  
946 swot-type observations using variational data assimilation and the full saint-venant hydraulic model. *Journal*  
947 *of Hydrology*, Accepted, to appear.
- 948 Paiva, R. C. D., Collischonn, W., Bonnet, M.-P., de Gonçalves, L. G. G., Calmant, S., Getirana, A., & Santos da  
949 Silva, J. (2013). Assimilating in situ and radar altimetry data into a large-scale hydrologic-hydrodynamic model  
950 for streamflow forecast in the amazon. *Hydrology and Earth System Sciences*, 17(7), 2929–2946. Retrieved from  
951 <https://hess.copernicus.org/articles/17/2929/2013/> doi: 10.5194/hess-17-2929-2013
- 952 Paris, A., Dias de Paiva, R., Santos da Silva, J., Medeiros Moreira, D., Calmant, S., Garambois, P.-A., ... Seyler,  
953 F. (2016). Stage-discharge rating curves based on satellite altimetry and modeled discharge in the amazon basin.  
954 *Water Resources Research*, 52(5), 3787-3814. Retrieved from [https://agupubs.onlinelibrary.wiley.com/](https://agupubs.onlinelibrary.wiley.com/doi/abs/10.1002/2014WR016618)  
955 [doi/abs/10.1002/2014WR016618](https://agupubs.onlinelibrary.wiley.com/doi/abs/10.1002/2014WR016618) doi: <https://doi.org/10.1002/2014WR016618>
- 956 Pavelsky, T. M. (2014). Using width-based rating curves from spatially discontinuous satellite imagery to monitor  
957 river discharge. *Hydrological Processes*, 28(6), 3035-3040. Retrieved from [https://onlinelibrary.wiley.com/](https://onlinelibrary.wiley.com/doi/abs/10.1002/hyp.10157)  
958 [doi/abs/10.1002/hyp.10157](https://onlinelibrary.wiley.com/doi/abs/10.1002/hyp.10157) doi: <https://doi.org/10.1002/hyp.10157>
- 959 Pontes, P. R. M., Fan, F. M., Fleischmann, A. S., de Paiva, R. C. D., Buarque, D. C., Siqueira, V. A., ...  
960 Collischonn, W. (2017). Mgb-iph model for hydrological and hydraulic simulation of large floodplain river  
961 systems coupled with open source gis. *Environmental Modelling & Software*, 94, 1-20. Retrieved from [https://](https://www.sciencedirect.com/science/article/pii/S136481521630189X)  
962 [www.sciencedirect.com/science/article/pii/S136481521630189X](https://www.sciencedirect.com/science/article/pii/S136481521630189X) doi: <https://doi.org/10.1016/j.envsoft>  
963 [.2017.03.029](https://doi.org/10.1016/j.envsoft.2017.03.029)
- 964 Pujol, L., Garambois, P.-A., Delenne, C., & Perrin, J.-L. (2024). Adjoint-based sensitivity analysis and assimilation  
965 of multi-source data for the inference of spatio-temporal parameters in a 2d urban flood hydraulic model. *In*  
966 *revision*.
- 967 Pujol, L., Garambois, P.-A., Delenne, C., & Perrin, J.-L. (2024). Adjoint-based sensitivity analysis and assimi-

968 tion of multi-source data for the inference of spatio-temporal parameters in a 2d urban flood hydraulic model.  
969 *submitted*.

970 Pujol, L., Garambois, P.-A., Finaud-Guyot, P., Monnier, J., Larnier, K., Mosé, R., ... Calmant, S. (2020).  
971 Estimation of multiple inflows and effective channel by assimilation of multi-satellite hydraulic signatures: The  
972 ungauged anabranching negro river. *Journal of Hydrology*, 591, 125331. Retrieved from [https://doi.org/](https://doi.org/10.1016/j.jhydrol.2020.125331)  
973 [10.1016/j.jhydrol.2020.125331](https://doi.org/10.1016/j.jhydrol.2020.125331)

974 Pujol, L., Garambois, P.-A., & Monnier, J. (2022). Multi-dimensional hydrological-hydraulic model with variational  
975 data assimilation for river networks and floodplains. *EGUsphere*, 2022, 1–44. Retrieved from [https://egusphere](https://egusphere.copernicus.org/preprints/egusphere-2022-10/)  
976 [.copernicus.org/preprints/egusphere-2022-10/](https://egusphere.copernicus.org/preprints/egusphere-2022-10/) doi: 10.5194/egusphere-2022-10

977 Rodríguez, E., Durand, M., & Frasson, R. P. d. M. (2020). Observing rivers with varying spatial scales. *Water*  
978 *resources research*, 56(9). Retrieved from <https://doi.org/10.1029/2019WR026476>

979 Roux, H. (2004). *Estimation de paramètres en hydraulique fluviale, à partir de données caractéristiques de l'imagerie*  
980 *aérienne* (Unpublished doctoral dissertation).

981 Samuels, P. G. (1989). Backwater lengths in rivers. *Proceedings of the Institution of Civil Engineers*, 87(4),  
982 571-582. Retrieved from <https://doi.org/10.1680/iicep.1989.3779> doi: 10.1680/iicep.1989.3779

983 Schneider, R., Godiksen, P. N., Villadsen, H., Madsen, H., & Bauer-Gottwein, P. (2017). Application of cryosat-2  
984 altimetry data for river analysis and modelling. *Hydrology and Earth System Sciences*, 21(2), 751–764. Retrieved  
985 from <https://hess.copernicus.org/articles/21/751/2017/> doi: 10.5194/hess-21-751-2017

986 Schuite, J., Flipo, N., Massei, N., Rivière, A., & Baratelli, F. (2019). Improving the spectral analysis of  
987 hydrological signals to efficiently constrain watershed properties. *Water Resources Research*, 55(5), 4043-  
988 4065. Retrieved from <https://agupubs.onlinelibrary.wiley.com/doi/abs/10.1029/2018WR024579> doi:  
989 10.1029/2018WR024579

990 Sobol', I., & Kucherenko, S. (2009). Derivative based global sensitivity measures and their link with global sensitivity  
991 indices. *Mathematics and Computers in Simulation*, 79(10), 3009-3017. doi: 10.1016/j.matcom.2009.01.023

992 Wongchuig-Correa, S., Cauduro Dias de Paiva, R., Biancamaria, S., & Collischonn, W. (2020). Assimilation of  
993 future swot-based river elevations, surface extent observations and discharge estimations into uncertain global  
994 hydrological models. *Journal of Hydrology*, 590, 125473. Retrieved from [https://www.sciencedirect.com/](https://www.sciencedirect.com/science/article/pii/S0022169420309331)  
995 [science/article/pii/S0022169420309331](https://www.sciencedirect.com/science/article/pii/S0022169420309331) doi: <https://doi.org/10.1016/j.jhydrol.2020.125473>

996 Yamazaki, D., Ikeshima, D., Sosa, J., Bates, P. D., Allen, G. H., & Pavelsky, T. M. (2019). Merit hydro: A high-  
997 resolution global hydrography map based on latest topography dataset. *Water Resources Research*, 55(6), 5053-  
998 5073. Retrieved from <https://agupubs.onlinelibrary.wiley.com/doi/abs/10.1029/2019WR024873> doi:  
999 <https://doi.org/10.1029/2019WR024873>

1000 Yoon, Y., Garambois, P.-A., Paiva, R. C., Durand, M., Roux, H., & Beighley, E. (2016). Improved error estimates  
1001 of a discharge algorithm for remotely sensed river measurements: Test cases on sacramento and garonne rivers.  
1002 *Water Resources Research*, 52(1), 278-294. Retrieved from [https://agupubs.onlinelibrary.wiley.com/doi/](https://agupubs.onlinelibrary.wiley.com/doi/abs/10.1002/2015WR017319)  
1003 [abs/10.1002/2015WR017319](https://agupubs.onlinelibrary.wiley.com/doi/abs/10.1002/2015WR017319) doi: <https://doi.org/10.1002/2015WR017319>

1004 Zanaga, D., Van De Kerchove, R., De Keersmaecker, W., Souverijns, N., Brockmann, C., Quast, R., ... Arino,  
1005 O. (2021, October). *Esa worldcover 10 m 2020 v100*. Zenodo. Retrieved from [https://doi.org/10.5281/](https://doi.org/10.5281/zenodo.5571936)  
1006 [zenodo.5571936](https://doi.org/10.5281/zenodo.5571936) doi: 10.5281/zenodo.5571936